ORIGINAL PAPER

The potential for practical improvements in cancer diagnostics by mathematically-optimized magnetic resonance spectroscopy

Dževad Belkić · Karen Belkić

Abstract   The fast Padé transform (FPT) has been benchmarked as a stable, high-resolution processor. In this paper, the performance of the FPT is examined for in vitro magnetic resonance (MR) spectroscopic data associated with ovarian, breast and prostate cancer as well as benign or normal tissue. We also examine how the FPT handles in vivo MR spectroscopic (MRS) time signals from human brain encoded by high field and clinical (1.5 T) scanners. Salient comparisons are made with the conventional data analysis through the fast Fourier transform (FFT). Separation of noise from genuine signal is carried out with a view to practical applications. Compared to the FFT, the fast Padé transform provided markedly improved resolution of total shape spectra from encoded in vivo time signals from healthy human brain and for in vitro data associated with ovarian cancer. Evidence is presented as to why it is necessary to go beyond MR total shape spectra to calculate metabolite concentrations. It is shown that error spectra, while necessary, are insufficient for accurate assessment of MR data. Two examples from oncology are given to illustrate this point: (1) a marker of breast cancer, phosphocholine, is detected on the component shape spectra, but not on the total shape spectrum, (2) diagnostically important multiplet resonances in prostate cancer spectra can only be detected on the component shape spectra, but not on the total shape spectrum. The FPT provides accurate calculation of metabolite

Dž. Belkić (✉) · K. Belkić
Department of Oncology/Pathology, Karolinska Institute, Building P-9, 2nd floor, P.O. Box 260,
17176 Stockholm, Sweden
e-mail: Dzevad.Belkic@ki.se

K. Belkić
School of Community and Global Health, Claremont Graduate University, Claremont, CA, USA

K. Belkić
Institute for Prevention Research, University of Southern California School of Medicine, Los Angeles,
CA, USA

concentrations based on in vitro MR data from three diagnostic problems in clinical oncology: (1) malignant and benign ovarian lesions, (2) breast cancer, fibroadenoma and normal breast tissue and (3) prostate cancer tissue, healthy glandular and stromal prostate tissue. Practical implementation of signal-noise separation is demonstrated for MR time signals encoded in vivo from the human brain on a clinical (1.5 T) scanner. Some 23 stable resonances are thereby identified and quantified. These results provide the basis for the needed next steps: to extensively apply the FPT to in vivo time signals encoded mainly on clinical scanners from e.g. brain tumors, breast, ovary and prostate cancers as well as from benign and normal tissue. The overall goal is that this practical approach through mathematical optimization enables Padé-based MRS to soon be implemented in clinical oncology, including target planning, post-radio-therapeutic follow-up and other aspects of radiation therapy.

Abbreviations

Ala	Alanine
AMARES	Advanced method for accurate robust and efficient spectral fitting
au	Arbitrary units
CDP	Cytosine diphosphate
Cho	Choline
Cit	Citrate
Cr	Creatine
Crn	Creatinine
FFT	Fast Fourier transform
FID	Free induction decay
FPT	Fast Padé transform
FWHM	Full width at half maximum
Glc	Glucose
Gln	Glutamine
GPC	Glycerophosphocholine
HLSVD	Hankel-Lanczos singular value decomposition
Iso	Isoleucine
Lac	Lactate
LCModel	Linear combination of model in vitro spectra
LP	Linear predictor
Lys	Lysine
Met	Methionine
m-Ins	Myoinositol
MR	Magnetic resonance
MRI	Magnetic resonance imaging
MRS	Magnetic resonance spectroscopy
MRSI	Magnetic resonance spectroscopic imaging
NMR	Nuclear magnetic resonance

PA   Polyamine
PCho   Phosphocholine
PE   Phosphoethanolamine
ppm   Parts per million
PSA   Prostate specific antigen
RT   Radiation therapy
s-Ins   Scylloinositol
SNR   Signal-to-noise ratio
SNS   Signal-noise separation
Tau   Taurine
tCho   Total choline
Thr   Threonine
Val   Valine
VARPRO   Variable projection method
ww   Wet weight

1 Introduction

Cancer diagnostics can potentially be improved on *a quantitative molecular basis* by retrieving key information that remains undetected with conventional data analysis, such as the fast Fourier transform (FFT) and post processing via fitting and/or peak integrations. The undetected information can be extracted by novel and self-contained data analysis, called the fast Padé transform (FPT), which has been introduced and benchmarked as the optimal method for magnetic resonance spectroscopy (MRS) [1–26]. This was made possible by widening the horizons of signal processing through finding its natural framework in a larger and well-established theory—quantum physics [1]. By identifying the quantification problem in signal processing as quantum-mechanical spectral analysis through the eigenvalue problem of the system's time evolution operator, the key door was opened for using a highly-developed mathematical apparatus in physics to overcome the otherwise insurmountable difficulties of the FFT, fittings and the like [7,8,10].

It is through this direct connection of signal processing with quantum physics that a *paradigm shift* has been established, by introducing the FPT as the method of choice for MRS. From the standpoint of mathematical modelling, the FPT is capable of extracting the missing information from the Fourier-analyzed time signals, because it has more degrees of freedom via the use of two polynomials in the form of their ratio P/Q rather than only one such polynomial encountered in the FFT. Mathematical modeling is indispensable in signal processing, since no encoded time signal can be interpreted directly without computations, in terms of the sought, clinically relevant information—the concentrations of metabolites from the tissue scanned by MRS.

The fast Padé transform meets the most stringent criteria imposed by clinical oncology for MRS [1–26]. The high resolution and stability of the FPT have been clearly confirmed in our studies of magnetic resonance (MR) total shape spectra [1–4,9,19,22], thereby overcoming one of the major Fourier-caused hindrances to wider application of MRS in clinical oncology. However, total shape spectra do not provide the

information needed to determine how many metabolite resonances are actually present in the tissue and in which concentrations. It is this latter information which is vital for improving the diagnostic yield and accuracy of MRS in oncology. Using the FPT, benchmark studies were performed in which the FPT was shown to provide *exact quantification* of MRS signals and thereby metabolite concentrations are reliably and unequivocally obtained with an intrinsic and robust error analysis [5,7–10].

It has also been demonstrated that the FPT unambiguously distinguishes genuine from spurious peaks in MRS spectra. The number of spurious resonances is always much larger than the number of genuine resonances. It is of utmost importance for trust-worthy clinical applications that the genuine information is identified with certainty by unmistakably disentangling it from noise. Via the concept of Froissart doublets (pole-zero cancellations), the FPT is shown to achieve this task [14,17–19,25]. In Refs. [17,20], we present the full mathematical derivation and demonstrate the exact reconstruction of the true number of genuine harmonics for noisy time signals or free induction decay (FID) curves with the pole-zero canonical form of the FPT. The *clinical significance* of this capability of the FPT is that, in practice, the MRS physical time signals are always corrupted with noise and the major problem is to identify the genuine resonances with fidelity.

In Refs. [7,12,19,20,26], validation is given for the computational algorithms by which the FPT yields quantitative spectral parameters. This is done without fitting and the solution is *unique*. Further, the FPT outperforms other parametric estimators, e.g. the linear predictor (LP) [27], Hankel-Lanczos Singular Value Decomposition (HLSVD) [28], etc. Likewise, the FPT outperforms all fitting techniques used in MRS: Variable Projection Method (VARPRO) [29], Advanced Method for Accurate Robust and Efficient Spectral fitting (AMARES) [30], Linear Combination of Model in vitro Spectra (LCModel) [31], etc.

Confidence in the FPT is built systematically by considering theoretically generated as well as experimentally encoded FIDs. We have performed computations [7,8] using the FPT to reconstruct spectral parameters for an MRS time signal that are associated with FIDs encoded on clinical scanners via proton MRS from the human brain [32,33]. Included in these successful reconstructions are not only isolated and closely overlapping resonances, but also those which are nearly degenerate. As will be shown in this paper, these latter resonances cannot possibly be detected via the total shape spectrum or error analysis through residual spectra—the difference between the input and the modeled spectra. Only the parametric analysis provided by e.g. FPT can detect and also exactly quantify such resonances, which are often of major clinical importance.

In this paper, we examine the performance of the FPT for in vitro data associated with ovarian, breast and prostate cancer as well as benign or normal tissue. We also examine how the FPT handles in vivo encoded MRS time signals from human brain from high field and clinical (1.5 T) scanners, with a focus upon separation of noise from genuine signal for practical applications. Salient comparisons are made with the FFT. These findings are viewed in relation to challenges in cancer diagnostics, particularly in radiation neuro-oncology regarding target definition and distinction of recurrent brain tumors form radiation necrosis. Recent work in optimization of radiation therapy (RT) through mathematical physics is also discussed in this light [25,34–39].

2 Data analysis

We use the polynomial quotient P_K/Q_K (diagonal) or P_{K-1}/Q_K (para-diagonal) as a rational function in harmonic variable $z^{-1} = \exp(-i\omega\tau)$, known in the literature as the Padé approximant. In signal processing, the Padé approximant is alternatively called the fast Padé transform [1,3] to highlight the possibility of obtaining a shape spectrum from an FID via a non-parametric estimation as reminiscent of the FFT. The latter type of estimation in the FPT is done by simply evaluating the Padé spectrum P_K/Q_K without ever searching for any of the spectral parameters that are the complex frequencies $\{\omega_k\}$ and amplitudes $\{d_k\}$. The FPT is the only parametric estimator which computes the envelope spectrum without the need to obtain the set $\{\omega_k, d_k\}$. The FPT is also used to perform parametric estimations by rooting the polynomial Q_K whose roots $\{z_k^{-1}\}$ yield $\{\omega_k\}$ and this readily leads to $\{d_k\}$ for each resonance. For example, the para-diagonal FPT treats the exact spectrum, i.e. the mentioned finite-rank Green function $G_N(z^{-1})$, via the *unique* ratio of two polynomials $P_{K-1}(z^{-1})/Q_K(z^{-1})$ at *any frequency* ω:

$$G_N(z^{-1}) = \frac{1}{N} \sum_{n=0}^{N-1} c_n z^{-n} \tag{1}$$

$$G_N(z^{-1}) \approx \frac{P_{K-1}(z^{-1})}{Q_K(z^{-1})} = \sum_{k=1}^{K} \frac{d_k}{z^{-1} - z_k^{-1}} \tag{2}$$

$$P_{K-1}(z^{-1}) = \sum_{r=0}^{K-1} p_r z^{-r}, \; Q_K(z^{-1}) = \sum_{s=0}^{K} q_s z^{-s}, \tag{3}$$

where $z = e^{i\omega\tau}$ and $z_k = e^{i\omega_k\tau}$. The para-diagonal $(L = K - 1)$ and diagonal $(L = K)$ Padé approximants are most frequently used from the set of the general Padé approximants, P_L/Q_K, because they incur minimal error in practice. In the FPT, the sum $\sum_{k=1}^{K} d_k/(z^{-1} - z_k^{-1})$ represents the complex-valued *total shape spectrum* (envelope) which is the sum of the K corresponding *component spectra*, $d_k/(z^{-1} - z_k^{-1})(1 \leq k \leq K)$. Here, P_{K-1} and Q_K are readily extracted from the input data G_N by treating the product $G_N Q_K$ in the defining relation $G_N * Q_K = P_{K-1}$ as a convolution.

We apply the FPT to reconstruct spectral parameters for the MRS time signals. Using the FPT to analyze these FIDs, the coefficients $\{p_r, q_s\}$ of the polynomials P_{K-1} and Q_K are computed efficiently by solving the systems of linear equations deduced from definition (1). Once $\{p_r, q_s\}$ are obtained, the (non-parametric) envelope spectrum can be computed by evaluating the quotient $P_{K-1}(z^{-1})/Q_K(z^{-1})$ at any selected frequency ω, as stated. To extract the peak parameters, one solves the characteristic equation $Q_K(z^{-1}) = 0$. This polynomial equation has K unique roots $z_k^{-1}(1 \leq k \leq K)$, so that the sought ω_k is deduced via $\omega_k = (i/\tau) \ln(z_k^{-1})$. A similar procedure applies to the diagonal FPT.

For reliable quantifications in MRS, it is not only the peak positions $\text{Re}(\omega_k)$ that count;[1] the peak widths $\text{Im}(\omega_k)$ and the complex amplitudes d_k are also critical. This is because the kth metabolite concentration is computed from the reconstructed peak parameters. From the spectral parameters, one can deduce the peak area underneath each resonance. Peak area is proportional to the concentration of the metabolite, relative to a selected reference concentration (water or another metabolite). Therefore, even for accurately determined ω_k's, the problem of obtaining the precise estimates of the d_k's becomes extremely important. In the FPT, the kth amplitude d_k depends only upon the kth root z_k^{-1} and it is obtained analytically from the Cauchy residue theorem [1]. When used as a parametric estimator, the FPT first finds all the peak parameters $\{\omega_k, d_k\}$ ($1 \leq k \leq K$) of every physical resonance *without ever using the Fourier spectrum*, or any other spectrum. A spectrum in the FPT is subsequently constructed in the absorption mode.

As in Ref. [8], a given reconstructed resonance can be identified as true versus spurious by computing a sequence of the Padé shape spectra $\{P_m/Q_m\}$ ($m = 1, 2, 3, \ldots$) in the frequency range of interest. Here, the fingerprint of detection of the exact number K of resonances is the attainment of the stabilization value $m = m'$ after which saturation is systematically maintained by observing that $P_{m'+q}/Q_{m'+q} = P_{m'}/Q'_m$ ($q = 1, 2, 3, \ldots$). This critical transition ($m = m'$) yields the sought K via $K = m'$, as verified to work in practice with MRS signals [8]. This is the concept of Froissart doublets, or equivalently, pole-zero cancellations [7,8]. The computation is carried out by gradually and systematically increasing the degree of the Padé polynomials. As these degrees change, the reconstructed spectra fluctuate until stabilization occurs. The value of the polynomial degree at which the predetermined level of accuracy is achieved represents the sought exact number of resonances K. This constancy of the reconstructed values can be obtained, e.g. via the cannonical representation of the Padé polynomial quotients:

$$\frac{P_{K-1}^{\pm}(z^{\pm 1})}{Q_K^{\pm}(z^{\pm 1})} = \frac{p_{K-1}^{\pm}}{q_K^{\pm}} \frac{\prod_{k=1}^{K-1} \left(z^{\pm 1} - \tilde{z}_k^{\pm}\right)}{\prod_{k'=1}^{K} \left(z^{\pm 1} - z_{k'}^{\pm}\right)}, \tag{4}$$

where $\tilde{z}_k^{\pm}$ and $z_k^{\pm}$ are the zeros of polynomials $P_{K-1}^{\pm}$ and $Q_K^{\pm}$, respectively.[2] The quotient form leads to cancellation of all the terms in the Padé numerator and denominator polynomials, when the computation is continued after the stabilized value of the order in the FPT has been attained, so that:

$$\frac{P_{K-1+m}^{\pm}(z^{\pm 1})}{Q_{K+m}^{\pm}(z^{\pm 1})} = \frac{P_{K-1}^{\pm}(z^{\pm 1})}{Q_K^{\pm}(z^{\pm 1})} \quad (m = 1, 2, 3, \ldots). \tag{5}$$

---

[1] Hereafter, $\text{Re}(u)$ and $\text{Im}(u)$ denote the real and imaginary parts of a complex number u.

[2] Hereafter, the superscripts $\pm$ indicate the two equivalent, complementary variants FPT$^{(\pm)}$ of the fast Padé transform operating inside and outside the unit circle $|z| < 1$ and $|z| > 1$, respectively.

The Cauchy residue of $P_{K-1}^{\pm}/Q_K^{\pm}$ from Eq. (5) represents the amplitudes $d_k^{\pm}$ whose analytical expressions are:

$$d_k^{\pm} = \frac{p_{K-1}^{\pm}}{q_K^{\pm}} \frac{\prod_{k'=1}^{K-1}(z_k^{\pm 1} - \tilde{z}_{k'}^{\pm})}{\prod_{k'=1,k'\neq k}^{K}(z_k^{\pm 1} - z_{k'}^{\pm})}. \tag{6}$$

Therefore, it is obvious from Eq. (7) that whenever $z_k^{\pm} = \tilde{z}_k^{\pm}$, the amplitudes $d_k^{\pm}$ of the poles from the Froissart doublets are exactly zero:

$$d_k^{\pm} = 0 \quad \text{for} \quad z_k^{\pm} = \tilde{z}_k^{\pm}. \tag{7}$$

For further details, see Refs. [17–19,24,25].

3 Results

3.1 Improved resolution of MR total shape spectra

3.1.1 In vivo MR spectra from healthy human brain encoded with high field scanners

In Fig. 1 we compare the performance of the FPT with the FFT for a clinical MRS signal obtained from an in vivo recording of the brain of a healthy volunteer, using the measured time domain data acquired at the static magnetic field strength of 4T. These data of full signal length $N = 2048$ were encoded by the group at the Center for Magnetic Resonance Research, University of Minnesota, Minneapolis, USA [33]. We present absorption spectra at three signal lengths, for the FFT (left column) and the FPT (right column). At the top panel of Fig. 1 the most dramatic differences between the FFT and FPT is seen at the shortest signal length ($N/16 = 128$). Here, the FFT presents no meaningful information, whereas nearly 90% of the NAA concentration is predicted by the peak at around 2.0 ppm by the FPT at ($N/16 = 128$). At one quarter signal length ($N/4 = 512$) on the middle left panel and at $N/2 = 1024$, the FFT has not demonstrated the accurate ratio between creatine and choline at 3.0 and 3.3 ppm, respectively; these two metabolites are still incorrectly appearing as almost equal. By contrast, for the FPT at one quarter signal length ($N/4 = 512$) on the middle right panel, the ratio of creatine to choline is correct, and remains so at half signal length ($N/2 = 1024$), on the bottom right panel. The triplet of glutamine and glutamate near 2.3 ppm can be discerned at half signal length only by the FPT, and not by the FFT. Therein, it can be seen that the FPT resolves with fidelity more than twenty metabolites, in which all peak parameters are accurately extracted, including the overlapping resonances [19]. Furthermore, while the FFT demands the total signal length ($N = 2048$) for convergence of the total shape spectrum, the difference between the two FPT spectra at $N = 1024$ and $N = 2048$ is buried entirely in the background noise [19]. In other words, in this illustration, the Padé-generated total shape spectrum at half-signal length can be treated as fully converged.

As seen in Fig. 1, the FPT produces no spurious metabolites or other spectral artefacts in the process of converging in a steady fashion as a function of the increased
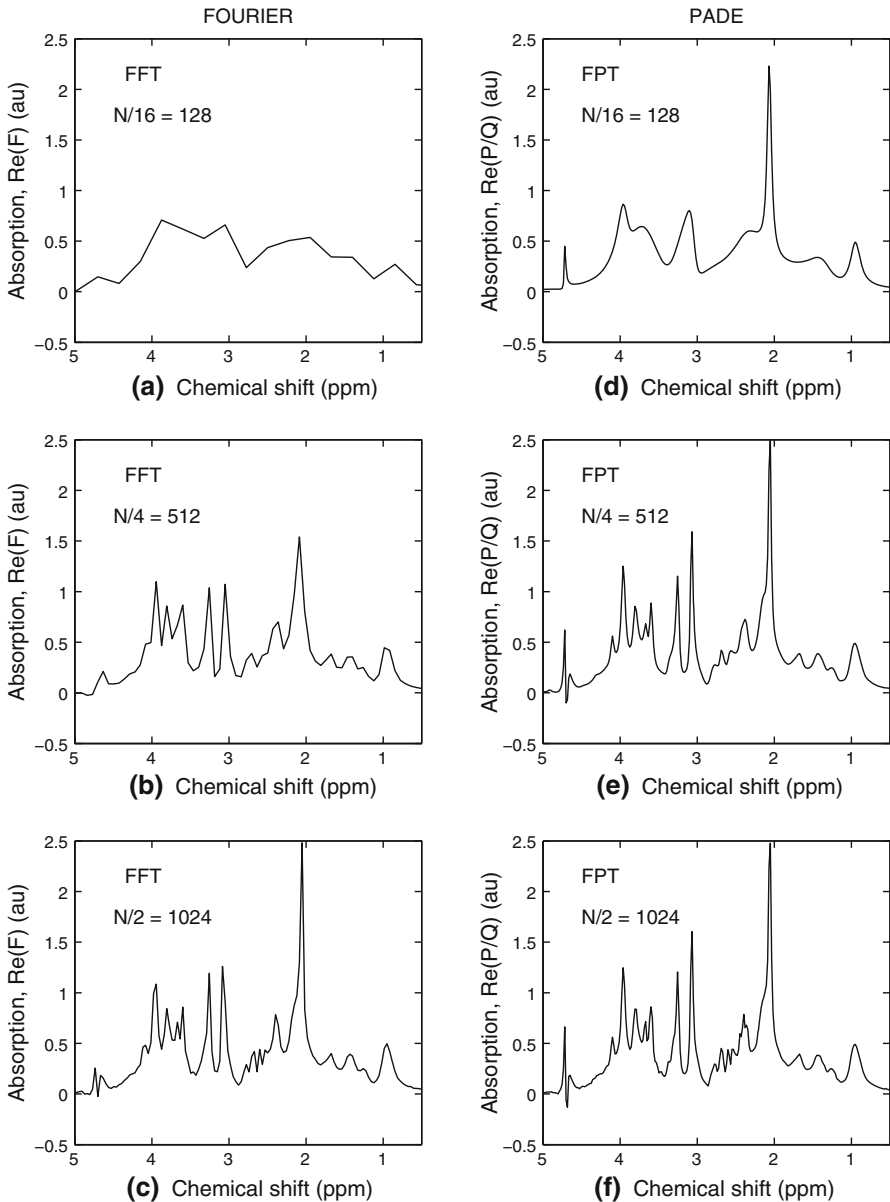
Fig. 1 Fourier and Padé absorption spectra computed using the time signal at three partial signal lengths ($N/16 = 128$, $N/4 = 512$, $N/2 = 1024$), where the full signal length is $N = 2048$, as encoded in Ref. [33] from occipital grey matter of a healthy volunteer. Hereafter, the abscissae are chemical shifts, as the relative dimensionless frequencies in part per million (ppm), and the ordinates are intensities in arbitrary units (au). Magnetic field strength: 4T

partial signal length. It is obvious that the FPT exhibits a much faster convergence rate than that in the FFT (for further illustrations see e.g. Refs. [2,3,19,23]). From a clinical standpoint, a particularly important message can be gleaned from Fig. 1. Namely, that the accuracy of the FFT is called into question, even with regard to semi-qualitative assessments such as metabolites ratios. It is upon these ratios e.g. creatine to choline that critical diagnostic determinations are often made, such as the distinction between recurrent brain tumor versus radiation necrosis [22].

3.1.2 Malignant ovarian lesions based upon in vitro MR data

Poor resolution and signal-to-noise ratio (SNR) have been major problems for in vivo MRS of the ovary [19,40]. In Fig. 2 the absorption spectra are displayed for malignant ovarian cyst data [40] at two signal lengths. The absorption spectra of the FFT (left panel) at $N/32 = 32$ (top (a)) and $N/16 = 64$ bottom (b)) are rough and uninterpretable. At $N/32 = 32$ (top right (c)), 9 of the 12 metabolites are resolved by the FPT. The remaining 3 resonances (isoleucine, threonine and the second resonance in the
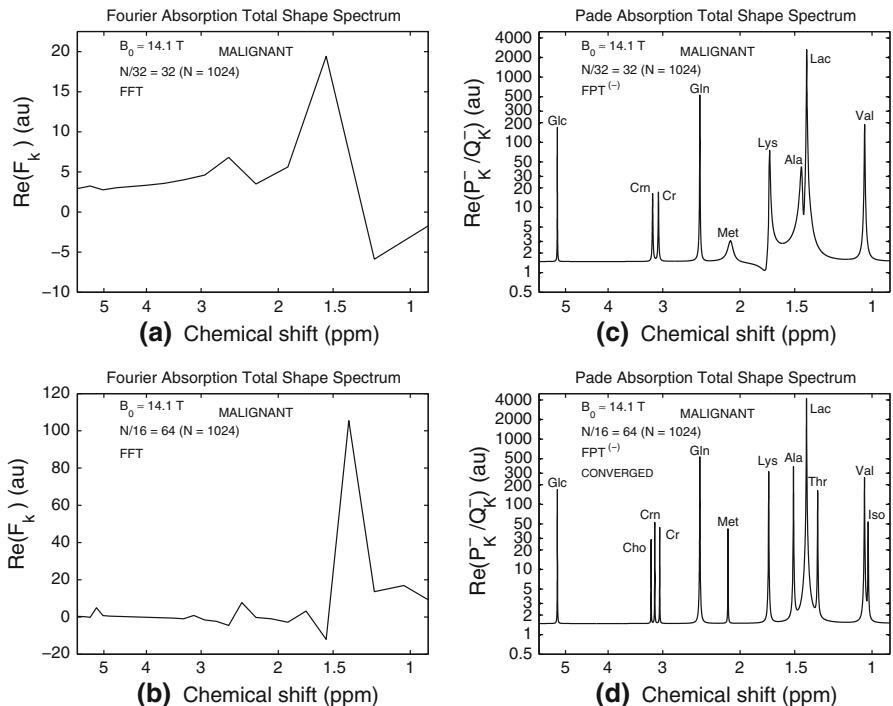

Fig. 2 Comparison of the resolution performance of the fast Fourier transform (FFT) (*left panels* **a**, **b**) and the fast Padé transform (FPT) (*right panels* **c**, **d**), for total absorption shape spectra of malignant ovarian cyst time signals from Ref. [40] at two short partial signal lengths. At $N/32 = 32$ signal points (*top panels*) the FFT (**a**) yields only a rudimentary spectrum with no discernable peaks, whereas the FPT (**c**) has resolved 9 of the 12 peaks. At $N/16 = 64$ signal points, the FFT (**b**) still has not adequately resolved any of the peaks, whereas the absorption spectrum from the FPT (**d**) is fully resolved, with the correct heights for all 12 peaks. Larmor frequency: 600 MHz (*see list of abbreviations for those corresponding to the metabolites*)

region between 3.1 and 3.2 ppm) need 64 signal points to be resolved by the FPT. All 12 metabolites are detected at $N/16 = 64$, and have the correct peak heights; thus the absorption spectrum is fully converged in the FPT at $N/16 = 64$ (bottom right (d)). The Padé-generated absorption spectra preserve convergence at longer fractions N/M ($M < 8$) of the full time signal including $N = 1024$ ($M = 1$) [11,13,19,23]. The FFT required $N = 8192$ signal points to resolve all 12 resonances. However, at that signal length, several peak heights were incorrect. This indicates that some of the metabolite concentrations estimated from the Fourier spectra by either fitting or peak integrations will be inaccurate even with 8192 signal points. The FFT actually needed 32768 signal points for convergence of the absorption total shape spectrum [11,13,19,23]. Thus, it is seen that advances in signal processing through the FPT markedly improve resolution of MR-visible metabolites characteristic of ovarian cancer.

3.2 The need to go beyond MR total shape spectra to calculate metabolite concentrations

3.2.1 Evidence that error spectra are insufficient

While the high-resolution capabilities of the FPT on the level of spectral envelopes are important for improving the diagnostic yield of MRS for oncology, it is essential to go beyond shape spectra to compute metabolite concentrations. The total shape spectrum provides qualitative information, but *not* how many metabolites underlie each peak or the relative strength of each component. At best, the FFT takes us only to this qualitative 2nd step. More information is needed before the metabolites can be identified and concentrations reliably determined; from the total shape spectrum this can only be guessed. This point is illustrated by a critical assessment of the information provided by error spectra. In MRS, error spectra are obtained by subtracting the absorption total shape spectra for the full signal length from those for the partial lengths. However, in Fig. 3 we show that while obtaining the residual or error spectra at the level of background noise may be a necessary condition, this is not sufficient for judging the reliability of estimation. The left column in Fig. 3 displays the Padé absorption component and total shape spectra, superimposed on top of each other at partial signal lengths $N_P = 180, 220, 260$. This is particularly illuminating when such shape spectra are juxtaposed to the corresponding three consecutive difference spectra on the right column in Fig. 3. Three consecutive difference spectra, built from the corresponding total shape spectra, are seen as all being identical to zero, on panels (d), (e) and (f) in Fig. 3, despite the lack of convergence of the component shape spectrum from panel (a) in the same figure. Therefore, it is recommended to pass beyond the point where full convergence of the total shape spectra has been reached for the first time (in this case we must surpass $N_P = 180$) in order to verify that anomalies do not occur in the final results. Such final results are obtained for $N_P = 220$ and 260 displayed on panels (b) and (c) for the components as well as for the envelopes. Clearly, monitoring the stability of the component spectra should be done in concert with inspection of the constancy of the reconstructed genuine spectral parameters [19,24].

Error Analysis in FPT via Shape Spectra (Component & Total: Left, Residual: Right); FID Length: N_P=180,220,260

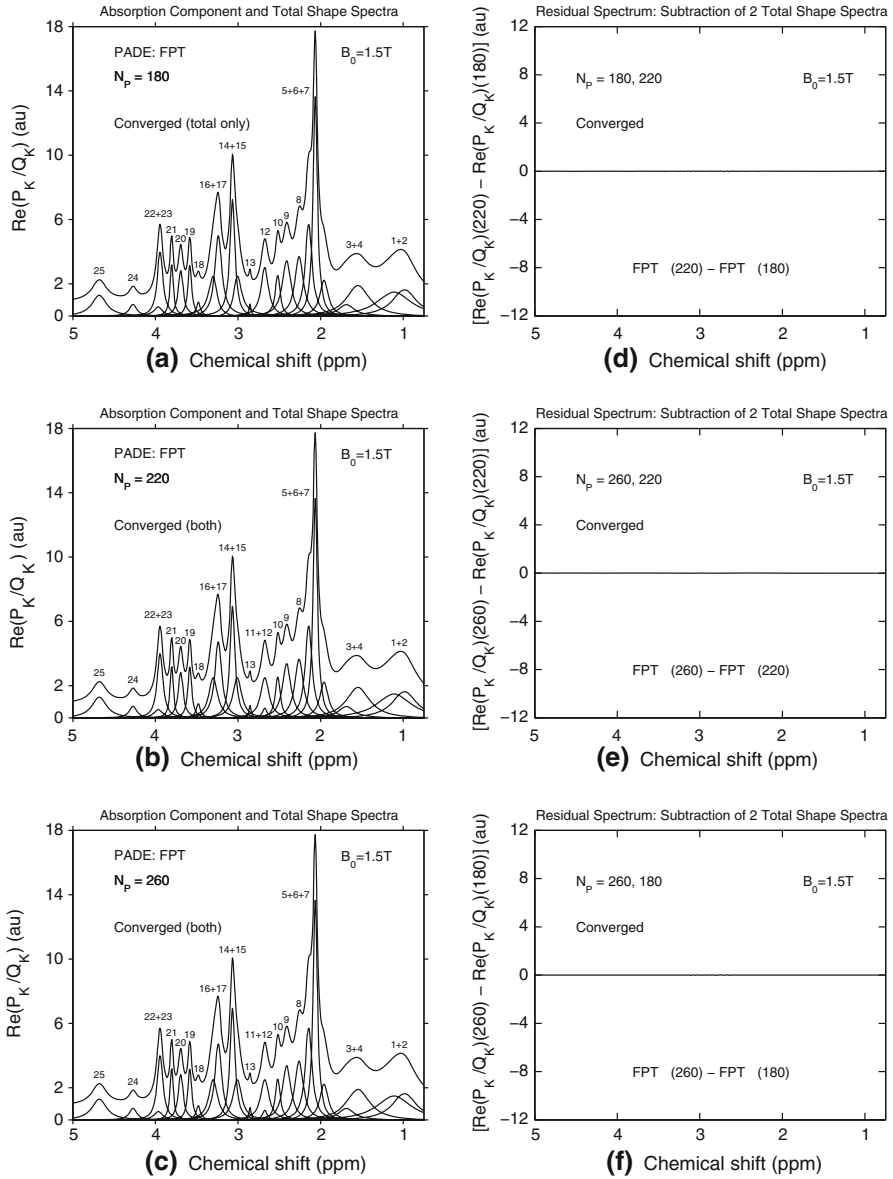**Fig. 3** *Left*: Absorption total shape spectra superimposed on *top* of the corresponding component shape spectra in the FPT near full convergence for signal lengths $N_P = 180, 220, 260$. *Right*: Consecutive difference spectra for absorption total shape spectra in the FPT for signal lengths $N_P = 180, 220, 260$. Magnetic field strength: 1.5 T

3.2.2 Key example #1 for oncology: a marker of breast cancer, phosphocholine, detected on the component shape spectra, but not on the total shape spectrum

In Fig. 4, we illustrate the clinical importance for breast cancer diagnostics of obtaining the component spectra. The absorption component shape spectra (left panels) and the total shape spectra (right panels) reconstructed by the FPT are shown at two partial signal lengths $N_P = 1000$ and $N_P = 1500$ for malignant breast data associated with in vitro time signals encoded by Gribbestad et al. [41]. These spectra are zoomed into the region between 3.2 and 3.3 ppm. Therein, it is most striking that phosphocholine and phosphoethanolamine are almost completely overlapping, separated by only about 0.0002 ppm, but nevertheless at convergence, the FPT can reconstruct the spectral parameters for these two resonances. At $N_P = 1000$, as seen on the top right panel (c), the absorption total shape spectrum is converged. However, this was not the case for the component shape spectrum (top left panel (a)), which at 3.22 ppm, shows the unresolved sum of peaks: #4 (PCho) and #5 (PE). At $N_P = 1500$ in the bottom left panel (b) of Fig. 4, the component shape spectrum is converged, with both peaks ##4
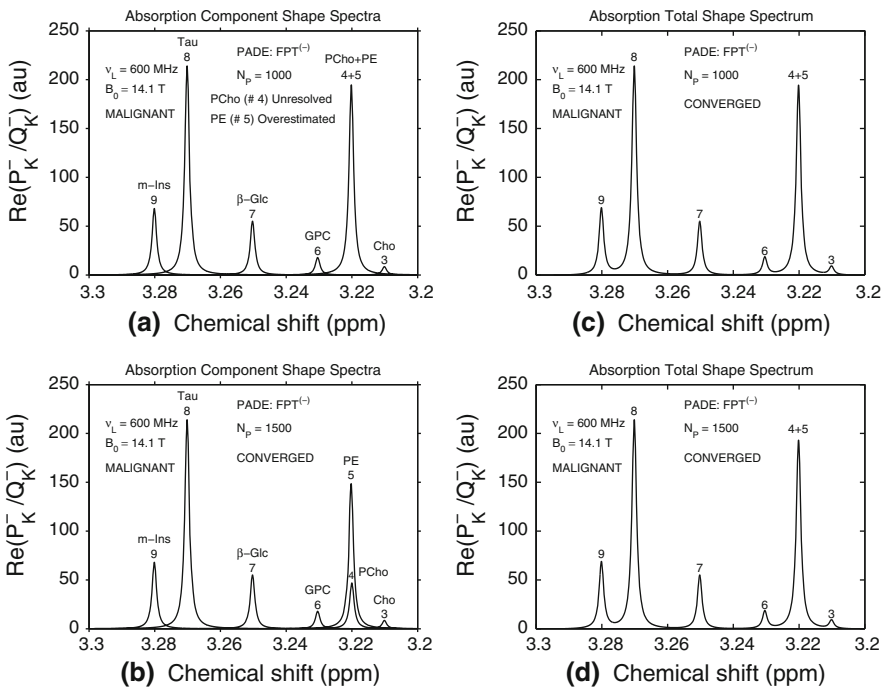

Fig. 4 Absorption component shape spectra (*left panels* **a**, **b**) and total shape spectra (*right panels* **c**, **d**) as reconstructed by the fast Padé transform for breast cancer from in vitro data of Ref. [41] zoomed within the interval of 3.2–3.3 ppm. At partial signal length $N_P = 1000$ the total shape spectrum (*panel* **c**) is converged, but the component spectrum (*panel* **a**) has not resolved PCho and has overestimated the height of phosphoethanolamine PE. At partial signal length $N_P = 1500$ (*bottom panels* **b**, **d**) the two resonances PCho and PE at 3.22 ppm are resolved with the correct heights. The PCho peak completely underlies PE. Larmor frequency: 600 MHz (*see list of abbreviations for those corresponding to the metabolites*)

and 5 resolved and having the correct heights, as was the case for all the other peaks in the region between 3.2 and 3.3 ppm. The PCho peak completely underlies PE.

Data from human breast cell lines research reveal that a "glycerophosphocholine to phosphocholine switch" occurs with malignant transformation [42], associated with over-expression of the enzyme choline kinase responsible for PCho synthesis [43,44]. This reflects changes in membrane choline phospholipid metabolism. The main steps in choline metabolism proceed via the cytosine diphosphate (CDP)-choline pathway [44]. Within that pathway, choline (3.21 ppm), PCho (3.22 ppm) and glycerophosphocholine (GPC) (3.23 ppm) can be visualized in the proton magnetic resonance spectrum. Thus, it is necessary to analyze the relationship among these closely overlapping resonances. When these three metabolites are summed up as "total choline" (tCho), as is conventionally done with in vivo MRS, salient information for breast cancer diagnostics could well be missed.

3.2.3 Key example #2 for oncology: multiplet resonances in prostate cancer spectra

For prostate cancer diagnostics, the importance of evaluating the component spectra is illustrated in Fig. 5A and B showing Padé reconstruction based upon encoded in vitro time signals from Ref. [45]. In Fig. 5A, there are numerous multiplet resonances, including the doublet of polyamine (components 8 and 9) and two citrate doublets (components 3–6) as well as two triplets of myoinositol (m-Ins) (components 20–25) and of taurine (tau) (components 13–15 and 17–19). These components can only be surmised from the total shape spectrum (Fig. 5B). When inspecting the total shape spectra alone, the true number of resonances underlying a given structure, their positions and relative intensity can merely be guessed. This is what is actually done by all the algorithms for post-processing via fitting that are used in the MRS literature [30,31], due to the reliance upon Fourier-based analysis, which can only provide a total shape spectrum. Using the FFT and fitting, the authors of Ref. [45] noted that spectral overlap was particularly problematic with regard to the accuracy of quantification for prostate spectra. In sharp contrast, we see that the FPT resolves multiplet resonances, including those for regions of otherwise very high spectral density that may best distinguish prostate cancer from normal tissue of different regions of the prostate.

3.3 Accurate calculation of metabolite concentrations based on in vitro MR data from three diagnostic problems in clinical oncology

3.3.1 Malignant and benign ovarian lesions

Not only does the FPT yield high-resolution shape spectra, but it also generates the parametric data from which metabolite concentrations can be reliably computed. With only 64 data points, the FPT exactly reconstructed the spectral parameters for all twelve metabolite peaks. Thereby, the metabolite concentrations were computed simply and unequivocally. Using the conventional Fourier approach, metabolite concentrations can only be estimated from the shape spectra by integrating the areas under the peaks.
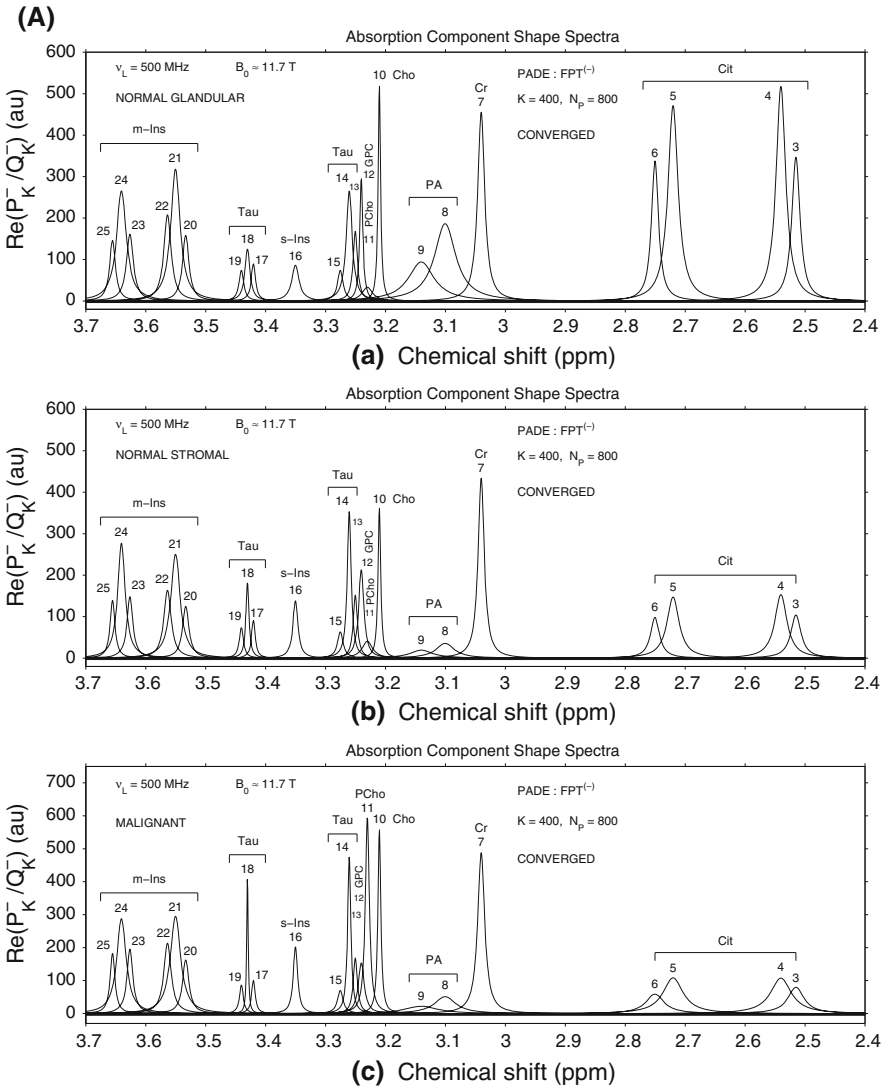
(A)

(a) Chemical shift (ppm)

(b) Chemical shift (ppm)

(c) Chemical shift (ppm)

Fig. 5 **A** Converged absorption component spectra reconstructed by the fast Padé transform at partial signal length $N_P = 800$, for normal glandular prostate (*top panel* **a**), normal stromal prostate (*middle panel* **b**) and malignant prostate (*bottom panel* **c**) within the region between 2.4 and 3.7 ppm derived from in vitro data of Ref. [45], **B** Converged absorption total shape spectra for the corresponding three cases, as reconstructed by the FPT. Abscissae are in ppm and ordinates are in arbitrary units (au). Larmor frequency: 500 MHz. (*see list of abbreviations for those corresponding to the metabolites*)

Even when the peaks are well delineated, there is still uncertainty about the lower and upper integration limits. If there are closely-lying peaks, this conventional approach for estimating metabolite concentrations becomes highly tenuous. Then, the "spectral crowding" problem severely hinders attempts at quantification [45,46]. The FPT generates the spectral parameters from which metabolite concentrations are accurately

(B)

(a) Chemical shift (ppm)

(b) Chemical shift (ppm)

(c) Chemical shift (ppm)
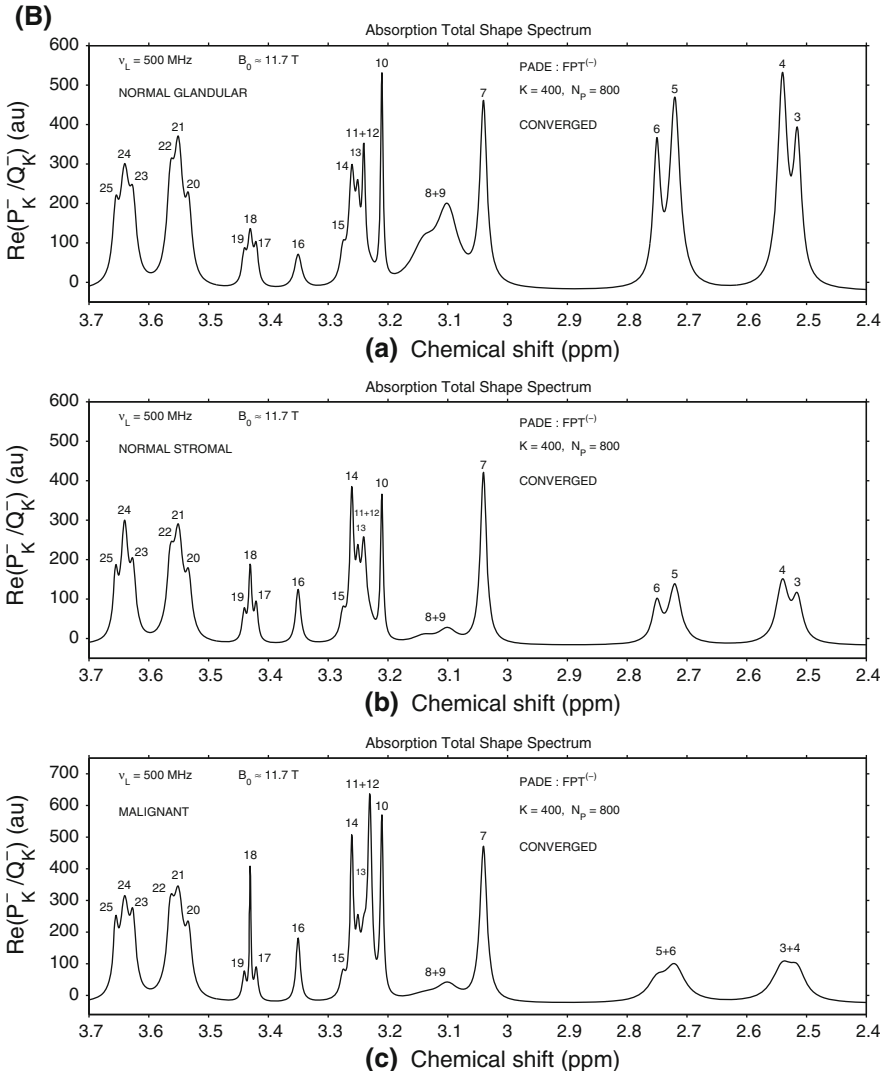
Fig. 5 continued

computed, whether or not the peaks are overlapping [7, 19]. Figure 6 shows the absorption spectra together with peak positions and retrieved concentrations, as achieved by the FPT at full convergence for the malignant ovarian (top panel (a)) and benign ovarian data (bottom panel (b)). The FPT thus performs both shape estimation and quantification without post-processing or reliance upon any other estimator. Figure 6 is particularly useful for clinicians, providing a graphic plus quantitative overview of malignant and benign ovarian cyst MRS data generated through reconstructions by the FPT.

Fig. 6 Summary of the clinically relevant quantitative data (peak positions and computed metabolite concentrations) together with the converged absorption total shape spectra, reconstructed by the fast Padé transform (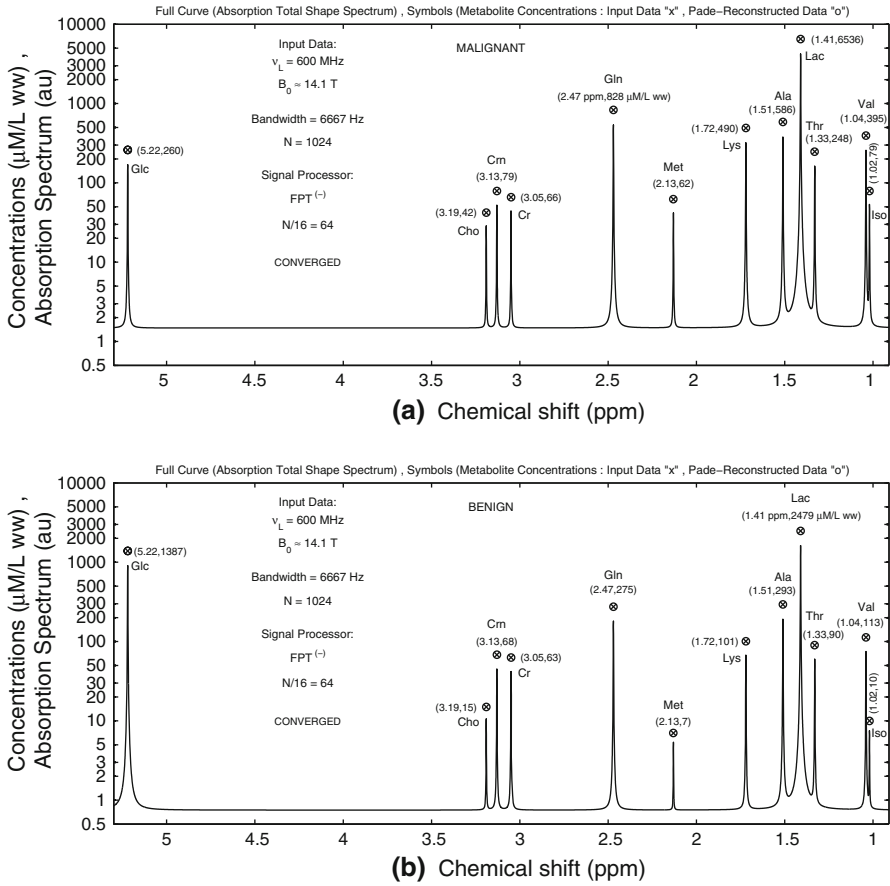FPT) for malignant ovarian cyst data from Ref. [40] (*top panel* **a**), and for benign ovarian cyst data (*bottom panel* **b**) from Ref. [40]. The metabolite concentrations are in μ M/L ww, where ww denotes wet weight. Larmor frequency: 600 MHz (*see list of abbreviations for those corresponding to the metabolites*)

3.3.2 Breast cancer, fibroadenoma and normal breast tissue

Figure 7 displays the converged metabolite maps reconstructed by the FPT for the normal breast tissue (top panel (a)), fibroadenoma (middle panel (b)) and for breast cancer (bottom panel (c)). For the normal breast tissue, lactate (#1), has the largest concentration ($0.5040 \, \mu$ M/g ww), slightly higher than β-glucose (#7) ($0.4500 \, \mu$ M/g ww). The median lactate concentration in the normal breast is about 0.34 of that in the fibroadenoma. For the malignant breast, the lactate concentration is over five times higher than in the fibroadenoma, and is clearly the largest resonance, nearly three time higher than taurine (#8). The capacity of the FPT to resolve and precisely quantify very closely overlapping resonances with certainty is clearly
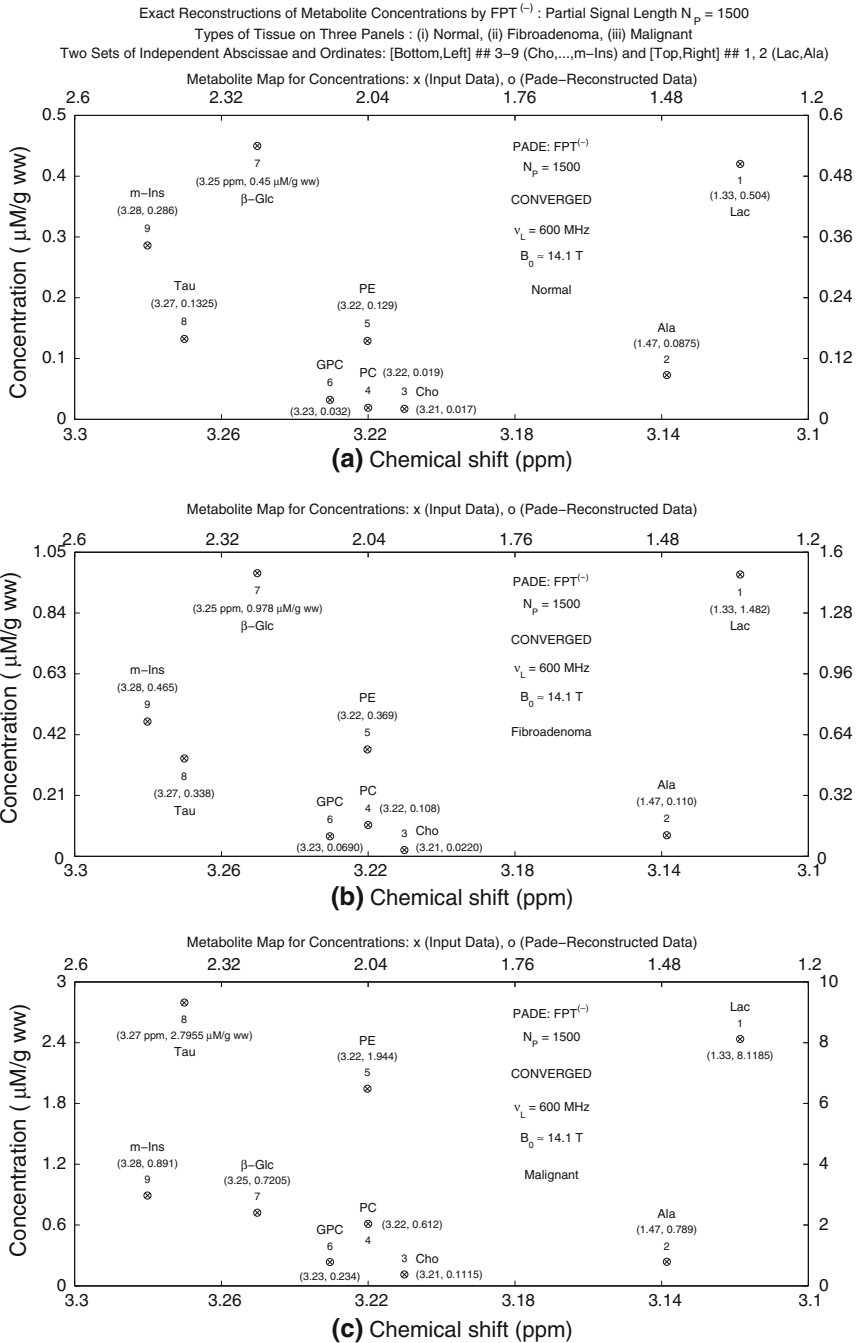
Fig. 7 Converged Padé-reconstructed metabolite concentrations ($N_P = 1500$) for normal breast tissue breast tissue (*top panel* **a**), fibroadenoma (*middle panel* **b**) and malignant breast (*bottom panel* **c**) derived from in vitro data of Ref. [41]. Larmor frequency: 600 MHz (*see list of abbreviations for those corresponding to the metabolites*)

demonstrated for the spectrally dense region between 3.21 and 3.23 ppm. This spectral region encompasses the constituents of tCho: choline at 3.21 ppm, PCho at 3.22 ppm and GPC at 3.23 ppm. Phosphocholine and PE are nearly completely overlapping at 3.22 ppm, separated by only 0.000203 ppm which is about four times less than the line widths. Nevertheless, at convergence, the FPT with full fidelity reconstructs the spectral parameters from which the concentrations of these two resonances are computed.

3.3.3 Prostate cancer tissue, healthy glandular and stromal prostate tissue

The Padé-reconstructed positions and peak heights, and the concentrations are presented in Tables 1 and 2 for two partial signal lengths in the middle and right columns, respectively. For the normal glandular prostate, prior to convergence at the partial signal length ($N_P = 600$), two peaks were unresolved: peak #11 PCho at 3.2302 ppm and peak #13 at 3.2503 ppm, which is one of the components of a taurine triplet. The heights of the two adjacent taurine (Tau) peaks ##14 and 15 were slightly overestimated, and their positions were resolved only to two decimal places. At $N_P = 600$ the concentration of GPC (peak #12) next to the missing PCho peak was overestimated by more than a factor of two. Most of the other retrieved concentrations were correct or nearly so, at that partial signal length. Full convergence was attained for the Padé-reconstructed peak parameters and concentrations for the normal glandular prostate data at $N_P = 700$ and remained stable at longer partial signal lengths, including the full signal length [16,19].

For normal stromal prostate, full convergence was reached at $N_P = 600$, as seen in the right column of Tables 1 and 2, and remained stable at longer partial signal lengths, including the full signal length [16,19]. Prior to convergence at $N_P = 500$, peaks ##11 and 13 at 3.2302 and 3.2503 ppm were unresolved. The peak heights of the adjacent components of the taurine triplet (peaks ##14 and 15) were somewhat overestimated, whereas at $N_P = 500$ the concentration of GPC, peak #12 was calculated to be nearly twice its correct value. Most of the other computed concentrations were close or equal to the correct values at $N_P = 500$. Thus, except that convergence occurred at a shorter signal length, the pattern for Padé-reconstruction of the normal stromal prostate data was similar to that for normal glandular prostate.

As was true for normal stromal prostate, Padé-reconstruction of the prostate cancer data reached convergence at $N_P = 600$, and remained stable at longer partial signal lengths, including the full signal length [16,19]. At $N_P = 500$, only one peak (#13) was unresolved, but the height of adjacent component (peak #14) of the taurine triplet was underestimated. Even though peak #11 (PCho) was resolved at that partial signal length and its height slightly overestimated, the concentration of the adjacent GPC peak (#12) was still overestimated by about a factor of two. Most of the other computed concentrations were either fully or approximately correct, prior to convergence at $N_P = 500$ for the Padé-reconstructed data from malignant prostate.

Thus, it is seen that the FPT accurately reconstructed all the sought spectral parameters for the data corresponding to the two types of normal prostate tissue and malignant prostate. Without any fitting or numerical integration of peak areas, the FPT thereby

Table 1 Input data for 12 metabolites for normal glandular prostate, normal stromal prostate and prostate cancer derived from Ref. [45] (left columns) and Padé-reconstructed peak position & heights and metabolite concentrations at two partial signal lengths (prior to convergence—middle columns and at full convergence—right columns)

		Input			Reconstructed prior to convergence			Reconstructed-converged		
		Position	Height	Concentration	Position	Height	Concentration	Position	Height	Concentration
Normal glandular prostate (i)	1. Lac	1.3302	7.3742	40.3	$N_P = 600$ 1.3302	7.3742	40.3	$N_P = 700$ 1.3302	7.3742	40.3
	2. Ala	1.4904	1.5791	8.63	1.4904	1.5773	8.62	1.4904	1.5791	8.63
	3. Cit	2.5152	1.5005	8.20	2.5152	1.5005	8.20	2.5152	1.5005	8.20
	4. Cit	2.5402	2.6167	14.3	2.5402	2.6167	14.3	2.5402	2.6167	14.3
	5. Cit	2.7202	2.5252	13.8	2.7202	2.5252	13.8	2.7202	2.5252	13.8
	6. Cit	2.7503	1.2443	6.80	2.7503	1.2443	6.80	2.7503	1.2443	6.80
	7. Cr	3.0403	1.6615	9.08	3.0403	1.6614	9.08	3.0403	1.6615	9.08
	8. PA	3.1004	2.1043	11.5	3.1004	2.1031	11.5	3.1004	2.1043	11.5
	9. PA	3.1403	1.2809	7.00	3.1403	1.2823	7.01	3.1403	1.2809	7.00
	10. Cho	3.2102	0.6441	3.52	3.2101	0.6436	3.52	3.2102	0.6441	3.52
	11. PCho	3.2302	0.1812	0.99	–	–	–	3.2302	0.1812	0.99
	12. GPC	3.2403	0.4684	2.56	3.2426	1.0661	5.83	3.2403	0.4684	2.56
Normal stromal prostate (ii)	1. Lac	1.3302	7.1546	39.1	$N_P = 500$ 1.3302	7.1546	39.1	$N_P = 600$ 1.3302	7.1546	39.1
	2. Ala	1.4904	1.2443	6.80	1.4904	1.2443	6.80	1.4904	1.2443	6.80
	3. Cit	2.5152	0.5599	3.06	2.5152	0.5599	3.06	2.5152	0.5599	3.06
	4. Cit	2.5402	0.9771	5.34	2.5402	0.9771	5.34	2.5402	0.9771	5.34
	5. Cit	2.7202	0.9442	5.16	2.7202	0.9442	5.16	2.7202	0.9442	5.16
	6. Cit	2.7503	0.4648	2.54	2.7503	0.4648	2.54	2.7503	0.4648	2.54
	7. Cr	3.0403	1.3962	7.63	3.0403	1.3962	7.63	3.0403	1.3962	7.63

Table 1 continued

	Input			Reconstructed prior to convergence			Reconstructed-converged		
	Position	Height	Concentration	Position	Height	Concentration	Position	Height	Concentration
8. PA	3.1004	0.3458	1.89	3.1004	0.3458	1.89	3.1004	0.3458	1.89
9. PA	3.1403	0.2306	1.26	3.1403	0.2300	1.26	3.1403	0.2306	1.26
10. Cho	3.2102	0.4959	2.71	3.2101	0.4984	2.72	3.2102	0.4959	2.71
11. PCho	3.2302	0.2214	1.21	–	–	–	3.2302	0.2214	1.21
12. GPC	3.2403	0.5727	3.13	3.2404	1.1122	6.08	3.2403	0.5727	3.13
Prostate cancer (iii)									
1. Lac	1.3302	11.0705	60.5	1.3302	11.0705	60.5	1.3302	11.0705	60.5
				$N_P = 500$			$N_P = 600$		
2. Ala	1.4904	2.3056	12.6	1.4904	2.3056	12.6	1.4904	2.3056	12.6
3. Cit	2.5152	0.6807	3.72	2.5152	0.6807	3.72	2.5152	0.6807	3.72
4. Cit	2.5402	1.1857	6.48	2.5402	1.1857	6.48	2.5402	1.1857	6.48
5. Cit	2.7202	1.1528	6.30	2.7202	1.1528	6.30	2.7202	1.1528	6.30
6. Cit	2.7503	0.5673	3.10	2.7503	0.5673	3.10	2.7503	0.5673	3.10
7. Cr	3.0403	1.7804	9.73	3.0403	1.7804	9.73	3.0403	1.7804	9.73
8. PA	3.1004	0.5801	3.17	3.1004	0.5803	3.17	3.1004	0.5801	3.17
9. PA	3.1403	0.3861	2.11	3.1402	0.3847	2.10	3.1403	0.3861	2.11
10. Cho	3.2102	0.8234	4.50	3.2102	0.8292	4.53	3.2102	0.8234	4.50
11. PCho	3.2302	1.2351	6.75	3.2300	1.2525	6.84	3.2302	1.2351	6.75
12. GPC	3.2403	0.4739	2.59	3.2464	0.9509	5.20	3.2403	0.4739	2.59

Positions are in parts per million, heights in arbitrary units, concentrations in μM/g ww. Metabolite abbreviations *Lac* lactate; *Ala* alanine; *Cit* citrate; *Cr* creatine; *PA* polyamine; *Cho* choline; *PCho* phosphocholine; *GPC* glycerophosphocholine; *Tau* taurine; *m-Ins* myoinositol; *s-Ins* scylloinositol

Table 2 Input data for normal glandular prostate, normal stromal prostate and prostate cancer derived from Ref. [45] (left columns) and Padé-reconstructed peak position & heights and metabolite concentrations at the indicated partial signal lengths (prior to convergence-middle columns and at full convergence—right columns) (peaks #13–27)

	Input			Reconstructed prior to convergence			Reconstructed-converged		
Position	Height	Concentration		Position	Height	Concentration	Position	Height	Concentration
Normal glandular prostate (i)				$N_P = 600$			$N_P = 700$		
13. Tau	3.2503	0.3843	2.10		–	–	–	3.2503	0.3843	2.10
14. Tau	3.2604	0.8234	4.50		3.2624	0.8654	4.73	3.2604	0.8234	4.50
15. Tau	3.2754	0.2196	1.20		3.2743	0.2543	1.39	3.2754	0.2196	1.20
16. s-Ins	3.3501	0.3312	1.81		3.3501	0.3309	1.81	3.3501	0.3312	1.81
17. Tau	3.4203	0.2013	1.10		3.4204	0.2081	1.14	3.4203	0.2013	1.10
18. Tau	3.4302	0.3294	1.80		3.4303	0.3132	1.71	3.4302	0.3294	1.80
19. Tau	3.4405	0.1830	1.00		3.4404	0.1910	1.04	3.4405	0.1830	1.00
20. m-Ins	3.5332	0.5343	2.92		3.5332	0.5356	2.93	3.5332	0.5343	2.92
21. m-Ins	3.5503	1.5572	8.51		3.5503	1.5512	8.48	3.5503	1.5572	8.51
22. m-Ins	3.5636	0.7960	4.35		3.5636	0.7995	4.37	3.5636	0.7960	4.35
23. m-Ins	3.6264	0.5892	3.22		3.6264	0.5873	3.21	3.6264	0.5892	3.22
24. m-Ins	3.6404	1.3742	7.51		3.6404	1.3774	7.53	3.6404	1.3742	7.51
25. m-Ins	3.6554	0.4447	2.43		3.6554	0.4440	2.43	3.6554	0.4447	2.43
26. m-Ins	4.0702	0.9625	5.26		4.0702	0.9625	5.26	4.0702	0.9625	5.26
27. Lac	4.1201	1.1345	6.20		4.1201	1.1343	6.20	4.1201	1.1345	6.20
Normal stromal prostate (ii)				$N_P = 500$			$N_P = 600$		
13. Tau	3.2503	0.3294	1.80		–	–	–	3.2503	0.3294	1.80
14. Tau	3.2604	0.7081	3.87		3.2620	0.7651	4.18	3.2604	0.7081	3.87
15. Tau	3.2754	0.1885	1.03		3.2737	0.2663	1.46	3.2754	0.1885	1.03
16. s-Ins	3.3501	0.3641	1.99		3.3502	0.3643	1.99	3.3501	0.3641	1.99
17. Tau	3.4203	0.1757	0.96		3.4201	0.1655	0.91	3.4203	0.1757	0.96
18. Tau	3.4302	0.2873	1.57		3.4304	0.3046	1.66	3.4302	0.2873	1.57
19. Tau	3.4405	0.1592	0.87		3.4404	0.1533	0.84	3.4405	0.1592	0.87
20. m-Ins	3.5332	0.4209	2.30		3.5333	0.4202	2.30	3.5332	0.4209	2.30

Table 2 continued

	Input			Reconstructed prior to convergence			Reconstructed-converged		
	Position	Height	Concentration	Position ($N_P = 500$)	Height	Concentration	Position ($N_P = 600$)	Height	Concentration
21. m-Ins	3.5503	1.2260	6.70	3.5503	1.2287	6.71	3.5503	1.2260	6.70
22. m-Ins	3.5636	0.6258	3.42	3.5637	0.6242	3.41	3.5636	0.6258	3.42
23. m-Ins	3.6264	0.4630	2.53	3.6264	0.4626	2.53	3.6264	0.4630	2.53
24. m-Ins	3.6404	1.0814	5.91	3.6404	1.0817	5.91	3.6404	1.0814	5.91
25. m-Ins	3.6554	0.3513	1.92	3.6554	0.3513	1.92	3.6554	0.3513	1.92
26. m-Ins	4.0702	0.7539	4.12	4.0702	0.7539	4.12	4.0702	0.7539	4.12
27. Lac	4.1201	1.0979	6.00	4.1201	1.0979	6.00	4.1201	1.0979	6.00
Prostate cancer (iii)									
13. Tau	3.2503	0.3641	1.99	—	—	—	3.2503	0.3641	1.99
14. Tau	3.2604	0.7813	4.27	3.2615	0.6252	3.42	3.2604	0.7813	4.27
15. Tau	3.2754	0.2086	1.14	3.2748	0.2888	1.58	3.2754	0.2086	1.14
16. s-Ins	3.3501	0.4593	2.51	3.3501	0.4589	2.51	3.3501	0.4593	2.51
17. Tau	3.4203	0.1903	1.04	3.4201	0.1871	1.02	3.4203	0.1903	1.04
18. Tau	3.4302	0.3129	1.71	3.4304	0.3098	1.69	3.4302	0.3129	1.71
19. Tau	3.4405	0.1738	0.95	3.4403	0.1803	0.98	3.4405	0.1738	0.95
20. m-Ins	3.5332	0.5490	3.00	3.5332	0.5477	2.99	3.5332	0.5490	3.00
21. m-Ins	3.5503	1.6011	8.75	3.5503	1.6054	8.77	3.5503	1.6011	8.75
22. m-Ins	3.5636	0.8179	4.47	3.5636	0.8155	4.46	3.5636	0.8179	4.47
23. m-Ins	3.6264	0.6112	3.34	3.6264	0.6115	3.34	3.6264	0.6112	3.34
24. m-Ins	3.6404	1.4254	7.79	3.6404	1.4250	7.79	3.6404	1.4254	7.79
25. m-Ins	3.6554	0.4611	2.52	3.6554	0.4612	2.52	3.6554	0.4611	2.52
26. m-Ins	4.0702	0.9936	5.43	4.0702	0.9936	5.43	4.0702	0.9936	5.43
27. Lac	4.1201	1.7017	9.30	4.1201	1.7017	9.30	4.1201	1.7017	9.30

See foot note of Table 1

provided reliable retrieved data for computation of the metabolite concentrations that could be better distinguish non-cancerous from malignant prostate. This was achieved at short signal lengths, which implies that problems due to Fourier-limited poor resolution are circumvented.

3.4 Signal-noise separation

3.4.1 Reliable quantification of noisy MR time signals for in vivo data encoded from human brain

Within the FPT, pole-zero cancellation (Froissart doublets) is used to distinguish genuine from spurious resonances. This is demonstrated here for typical noisy MR time signals. Our paper [17] provides an in-depth examination of the most challenging numerical aspects for solving the quantification problem in MRS. Specifically, we show that when the FPT is close to the convergence region, an unprecedented phase transition occurs, since literally a couple of additional signal points are sufficient to reach full accuracy. As illustrated earlier in Fig. 3, residual spectra are a necessary, but not sufficient criterion to estimate the error invoked in quantification.

We emphasize that our proof for this principle becomes of critical importance to solving the quantification problem of very closely overlapping resonances that arise in the applications of the FPT to MRS signals in breast and prostate cancer. While accuracy, resolving power, convergence rate and robustness of any signal processor depend on such obvious parameters as the signal-to-noise ratio and the total acquisition time of the investigated time signal, there are also a number of more subtle features of spectral analysis that play a key role in the performance of a given estimator. These include the configurations of the poles and zeros in the complex plane, their density in the selected portion of the Nyquist interval, the smallest distance among the poles and zeros, inter-separations among poles and zeros, their distance from the real axis and the smallest imaginary frequencies (the longest lifetimes of the resonance states). Among the most suitable mathematical tools for investigating these subtle effects are Argand plots which display the imaginary part as a function of the corresponding real part of any given complex-valued quantity. In MRS these graphs have special ramifications stemming from the concept of Froissart doublets, via their mechanism of pole-zero cancellations.

Figure 8 shows the results from the FPT for noisy MR time signals. The unique pole-zero cancellations for the Froissart doublets seen in the $FPT^{(+)}$ (top panel) and $FPT^{(-)}$ (middle panel) of Fig. 8, are simultaneously accompanied by zero-valued amplitudes (bottom panel) as another illustration of how the FPT distinguishes genuine from spurious resonances. The $FPT^{(+)}$ sharply separates the genuine from the spurious resonances in two different regions with positive and negative imaginary frequencies, respectively. This unprecedented separation of the physical from the unphysical informational content of the investigated data using the FPT plays a key role in optimally reliable spectral analysis for quantifications in MRS.
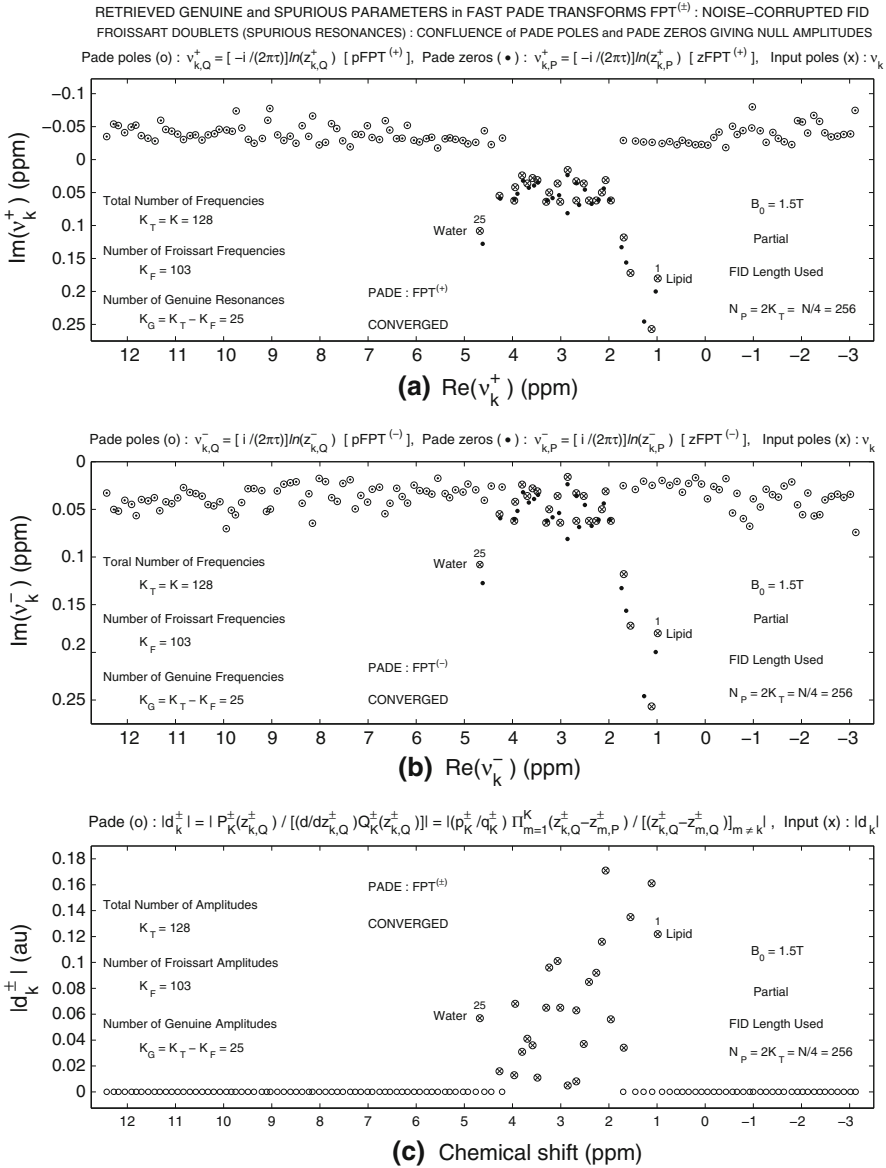
RETRIEVED GENUINE and SPURIOUS PARAMETERS in FAST PADE TRANSFORMS FPT$^{(\pm)}$: NOISE–CORRUPTED FID
FROISSART DOUBLETS (SPURIOUS RESONANCES) : CONFLUENCE of PADE POLES and PADE ZEROS GIVING NULL AMPLITUDES

Pade poles (o) : $\nu_{k,Q}^+ = [-i/(2\pi\tau)]ln(z_{k,Q}^+)$ [pFPT$^{(+)}$],   Pade zeros (•) : $\nu_{k,P}^+ = [-i/(2\pi\tau)]ln(z_{k,P}^+)$ [zFPT$^{(+)}$],   Input poles (x) : ν_k

(a) Re(ν_k^+) (ppm)

Pade poles (o) : $\nu_{k,Q}^- = [i/(2\pi\tau)]ln(z_{k,Q}^-)$ [pFPT$^{(-)}$],   Pade zeros (•) : $\nu_{k,P}^- = [i/(2\pi\tau)]ln(z_{k,P}^-)$ [zFPT$^{(-)}$],   Input poles (x) : ν_k

(b) Re(ν_k^-) (ppm)

Pade (o) : $|d_k^\pm| = |P_K^\pm(z_{k,Q}^\pm)/[(d/dz_{k,Q}^\pm)Q_K^\pm(z_{k,Q}^\pm)]| = |(p_K^\pm/q_K^\pm)\Pi_{m=1}^K(z_{k,Q}^\pm - z_{m,P}^\pm)/[(z_{k,Q}^\pm - z_{m,Q}^\pm)]_{m \neq k}|$,   Input (x) : $|d_k|$

(c) Chemical shift (ppm)

Fig. 8 Froissart doublets for unequivocal determination of the exact number K_G of the genuine frequencies and amplitudes from the total number $K_T \equiv K$ of the spectral parameters reconstructed by the FPT$^{(\pm)}$ for the FID corrupted with random Gaussian white noise. In *panel* **a**, the FPT$^{(+)}$ separates the genuine from spurious frequencies in the two non-overlapping regions. In *panel* **b** for the FPT$^{(-)}$, genuine and spurious frequencies are in the same region Im(ν_k^-)>0 where $\nu^\pm = \omega_k^\pm/(2\pi)$. In *panel* **c**, all the spurious (Froissart) amplitudes are unambiguously identified by their zero values. Magnetic field strength: 1.5 T

*3.4.2 Key step: practical implementation of SNS on MR time signals encoded
      in vivo from the human brain on a clinical (1.5 T) scanner*

In Fig. 9 we compare the performance of the FPT and the FFT on an MR time signal
or FID of length $N = 2048$, bandwidth=2500 Hz encoded in Ref. [47] from human
brain with a 1.5 T clinical scanner.

The top left panel (a) of Fig. 9 shows the encoded FID after experimental water
suppression. This is a complex-valued exponentially damped signal with the real and
imaginary parts as a function of time. On the top right panel (e) of Fig. 9, the time signal
is processed by the FFT in the full Nyquist range using all the FID points $N = 2048$.
It is seen that the residual water at 4.68 ppm is still the overwhelmingly dominant
peak. The remaining peaks for metabolites between 1 and 4 ppm are extremely small
relative to the water resonance.

The four middle panels of Fig. 9 compare convergence rates of the FFT (left panels
(b), (c)) and the FPT (right panels (f), (g)) at two partial signal lengths with the fixed
bandwidth. At $N/8 = 256$, the FFT provides only a rudimentary absorption total
shape spectrum. By contrast, in the FPT, N-acetyl aspartate at 2.0 ppm is close to its
correct form and Cho as well as Cr are clearly resolved. Full convergence is achieved
with the FPT at $N/2 = 1024$ (panel f), but not with the FFT (panel c). Most notably,
at half-signal length the ratio of Cho to Cr is incorrect with the FFT (as was the case
in Fig. 1 encoded at 4T). The FFT needs to exhaust the full signal length $N = 2048$
to converge.

The bottom panels (d, h) of Fig. 9 show the residual spectra: FFT at full signal
length ($N = 2048$) minus the FPT at two partial signal lengths. The FPT treats all
the physical metabolites on the same footing, including the enormous water peak. In
panel (d), [FFT ($N = 2048$) − FPT($N/8 = 256$)], it is seen that the FPT is starting to
converge. In other words, the information from panel (d) coheres well with the cor-
responding Padé-spectrum at $N/8 = 256$ in panel (f). The residual spectrum shown
in panel (h): [FFT ($N = 2048$) − FPT($N/2 = 1024$)] is at the level of background
noise and thus corroborates that the absorption total shape spectrum from the FPT has
indeed converged at half signal length.

Overall, as with FIDs encoded at high fields (4T, 7T) [1–3,9], the FPT outperforms
the FFT at 1.5 T by exhibiting a faster convergence rate and better resolving power. The
additional advantage of the FPT over the FFT is quantification. The displayed spectra
in the FPT have been computed by first extracting all the fundamental frequencies and
amplitudes. We unequivocally quantified 22 metabolites via the Signal-Noise Separa-
tion (SNS) procedure. By comparison, the LCModel via post-processing fitting of the
FFT spectra quantified only five metabolites [47]. This conclusion has been system-
atically confirmed with some 100 other spectra from healthy and pathological tissue
analysed in Ref. [48]. The leading role of the fast Padé transform in signal processing
is thereby further established.

Signal-noise suppression is illustrated in Fig. 10 from an MR time signal of length
$N = 2048$ encoded at the Karolinska Institute from the brain of a healthy volun-
teer. The top panel a displays the absorption total shape spectra, as initially computed
by the FFT and parametrically reconstructed by the FPT. These total shape spectra
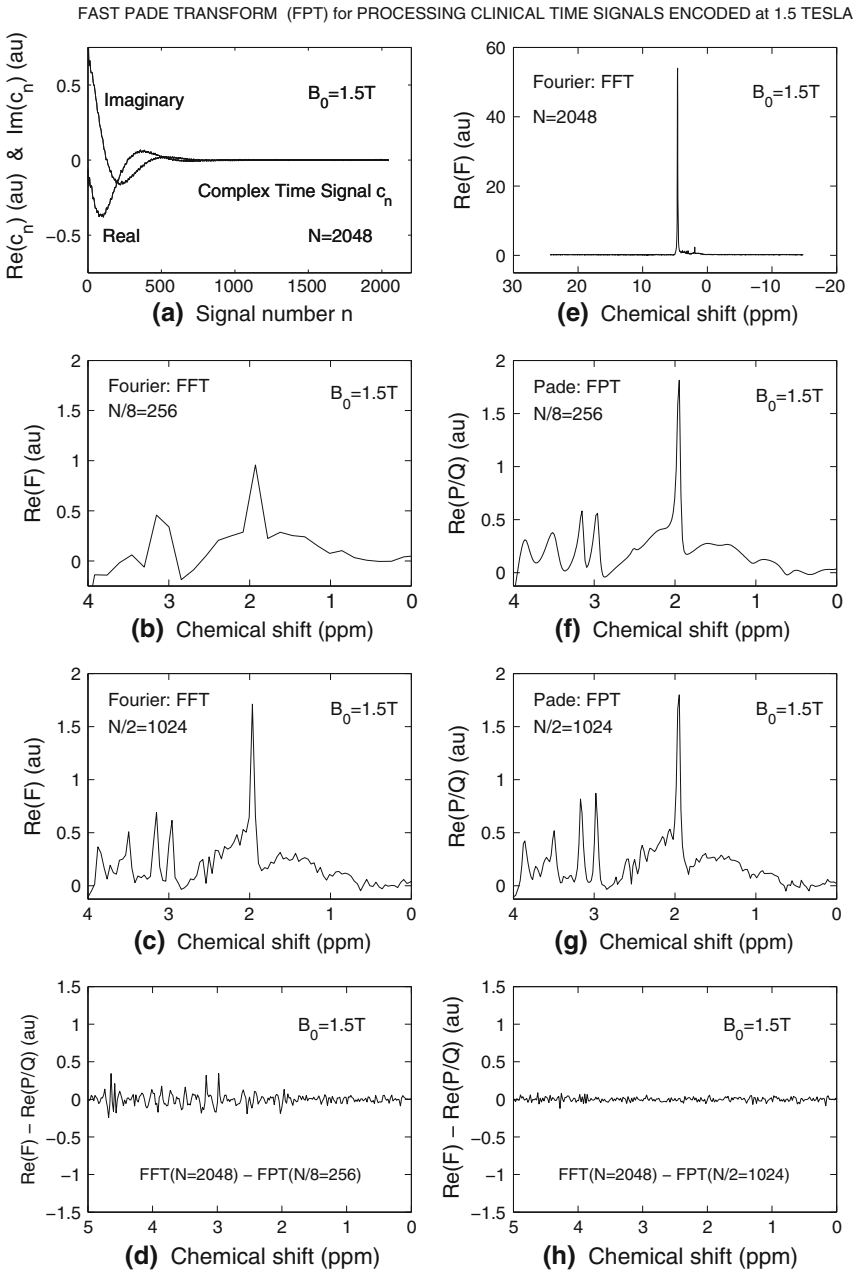contain genuine (physical) as well as spurious (unphysical, noisy) information. The

FAST PADE TRANSFORM (FPT) for PROCESSING CLINICAL TIME SIGNALS ENCODED at 1.5 TESLA

Fig. 9 Comparison of the performance of the FPT and the FFT on an MR time signal of length $N = 2048$, bandwidth = 2500 Hz encoded in Ref. [47] from the brain of a healthy volunteer with a 1.5 T clinical scanner. *Top left panel* **a** of shows the encoded FID after experimental water suppression. *Top right panel* **e**, the time signal processed by the FFT in the full Nyquist range at $N = 2048$. The *four middle panels* compare performance of the FFT (*left panels* **b**, **c**) and the FPT (*right panels* **f**, **g**) at partial signal lengths. The *bottom panels* (**d** and **h**) show the residual spectra: FFT at full signal length ($N = 2048$) *minus* the FPT at two partial signal lengths

formidable task is to separate the former from the latter, in order to reconstruct only the genuine spectral parameters (yielding metabolite concentrations, chemical shifts, relaxation times) as well as the component and total shape spectrum.

We effectively achieved the signal-noise separation, or SNS, by adding a few percent noise to the already noisy in vivo FID. In the illustration for Fig. 10, the FID is corrupted by random zero-mean 5% Gaussian white noise. Good statistics are secured by creating 50 different realizations of this noise by merely changing the input seed numbers to the computer's generator of random numbers. This gives 50 noisy FIDs of the same type, but comprised of different random numbers. When these different noisy sets, each of length $N = 2048$, are added (one at a time) to the original in vivo FID, 50 noise-corrupted FIDs are obtained. Each FID is subsequently subjected to parametric spectral analysis by the FPT. This method reconstructs 50 sets of frequencies and amplitudes. The retrieved averaged frequencies are plotted on panel b in Fig. 10, where the abscissa is chemical shift and the ordinate is full-width at half maximum in descending order. Panel c in Fig. 10 displays chemical shifts (abscissa) for each of the 50 sets/realizations (ordinates) of the fixed 5% random zero-mean Gaussian noise. It is seen that frequencies plotted with the filled squares are stable for every noise realization, whereas those associated with the open squares are unstable. Here, stability means that both positions (chemical shifts) and full width at half maximum (FWHM) are practically the same for all the 50 FIDs. Instability signifies that noticeable changes occur either in chemical shifts or in FWHMs or in both.

All stable resonances are seen to have fundamental frequencies (spectral poles) located relatively close to the real axis, and this yields narrow widths (longer lifetimes) of the related peaks or resonances in the absorption spectrum. Unstable poles roam around for each noise realization, especially when they are away from the real axis. For example, the most pronounced instability is the open square at 0.7 ppm from panel b and the associated widely wiggling symbols "x" (panel c) showing marked alterations in chemical shifts when passing from one to another realization of noise.

In this way, stable and unstable features can confidently be identified as physical and unphysical (noisy) contents of the original in vivo FID and the corresponding absorption spectrum. Stable poles are retained in the output of quantification and in the ensuing spectra, whereas all unstable poles are discarded (panel d). The bottom panel d displays the noise-reduced absorption total shape spectrum reconstructed by the FPT, which is, hence, exclusively based upon the stable, genuine poles. Strikingly, this final FPT-generated spectrum is significantly improved relative to the corresponding initial full line (signal + noise) in panel a.

The net improvement is in getting rid of instability through the stability plot in Fig. 10 or the SNS procedure. Note that most peaks in the initial spectrum from panel a are asymmetrical due to shimming imperfections. In the usual practice, such encoding artefacts are tackled by post-processing procedures, e.g. apodization (exponential damping), zero-order phase correction, etc. This phasing amounts to multiplication of the FFT-computed spectrum by $\exp(i\phi)$, where ϕ is an arbitrary angle chosen subjectively to partially diminish the distorting effect in the rolling baseline and, thus, to make the total shape Fourier spectrum look "nicer" and closer to symmetrical Lorentzian/Gaussian-type lineshapes. By contrast, the SNS procedure [14,17–19,25] is objective, since it relies on the stability of the physical characteristics of the
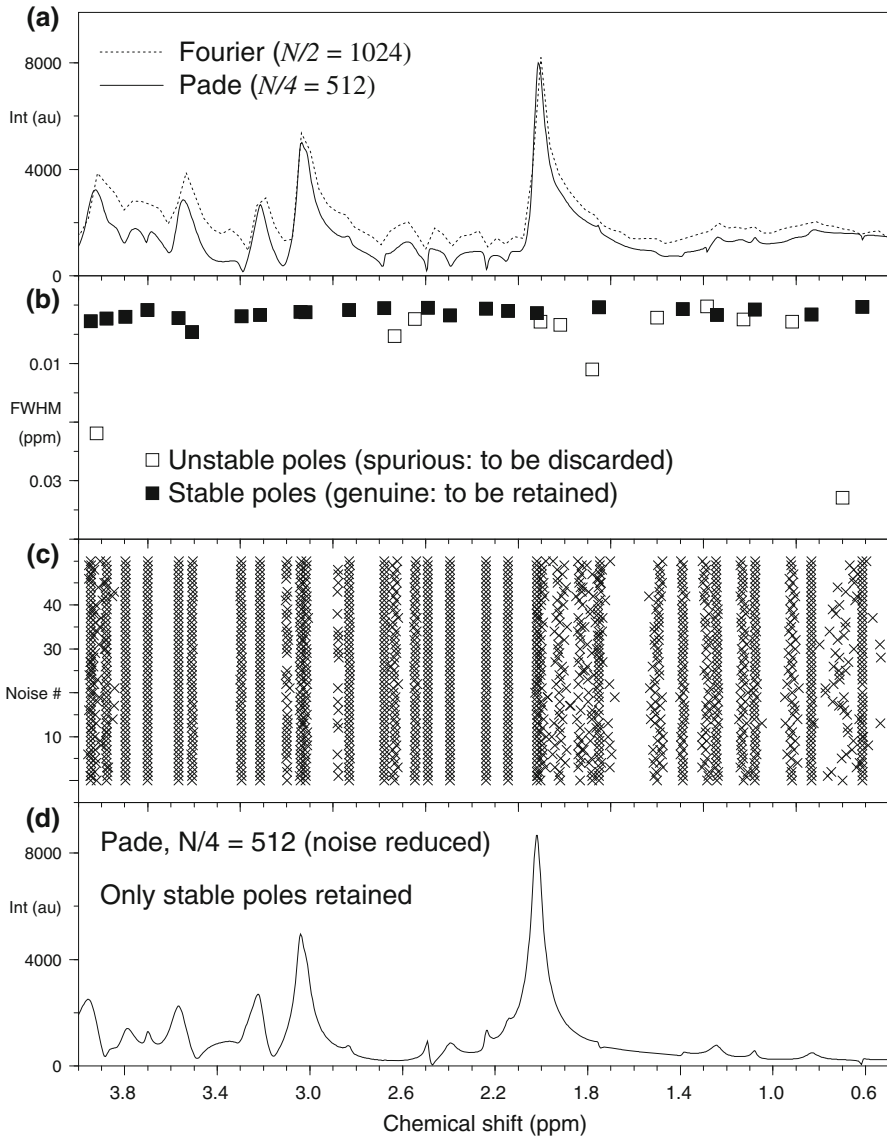
Fig. 10 "Stability Plots" for reconstructed spectral parameters: Abscissae on all panels (**a–d**) are chemical shifts, as resonating relative real frequencies in ppm. *Topmost panel* **a**: Absorption total shape spectra (envelopes), as reconstructed by the converged FPT (*full line*) and computed by the non-converged FFT (*dotted line*; convergence at $N = 2048$) with genuine and noisy information from an MR time signal encoded from the brain gray matter of a healthy volunteer. *Panel* **b**: identification and distinction of stable and unstable poles. *Panel* **c**: 50 sets/realizations (ordinates) of added fixed 5% random zero-mean Gaussian white noise. *Panel* **d**: Noise reduced total absorption shape spectrum, containing 23 stable resonances. Ordinate "Int" (au) on panels **a** and **d** is absorption intensity in arbitrary units (au). On panel **b**, the ordinate FWHM is the full width at half maximum (proportional to the imaginary fundamental frequencies)

analyzed in vivo FID. For example, an improper shimming during the calibration of the encoding system, which subsequently leads to asymmetrical peaks, is an extraneous spectral content whose spuriousness is expected to be manifested through instability, since such information is not an indigenous part of the original FID. By reference to the full lines of panels a and d in Fig. 10, this is precisely what is objectively detected via SNS. To summarize, via the SNS procedure, some 23 stable resonances are identified and quantified from an in vivo MR time signal encoded at 1.5 T. This illustrates the advantage and possibility for practical implementation of the FPT/SNS in the clinical setting. This should be contrasted to the usual practice of identifying only a handful of metabolites by means of post-processed FFT. Currently, even with ratios of concentrations from a few metabolites, MRS is viewed as a modality which could revolutionize cancer diagnostics [49,50]. This potential can be significantly enhanced by the expounded FPT/SNS strategy which consistently and reliably provides more than 20 metabolite concentrations with clinical 1.5 T scanners [20].

4 Discussion: importance of these results for oncology

Since MRS is increasingly recognized as a potentially key diagnostic modality in oncology [49–54], it is vital to overcome the shortcomings that hamper further clinical applications of MRS in cancer diagnostics. In order to achieve this, more advanced signal processing methods are needed, and it has now been demonstrated that the FPT is the signal processing method of choice to achieve this goal.

The established algorithmic success of the FPT emerges from fundamental principles linking signal processing to quantum physics. Poor resolution and the inability to separate noise from signal via FFT are major obstacles to data analysis and clinical data interpretation for MRS in oncology. The superior resolution, noise suppression and stability of the FPT for MRS signals are firmly and verifiably established [1–3,5–10,14,17–20,23–25].

Our benchmark studies show that the FPT can provide optimal quantification of MRS signals yielding reliable metabolite concentrations with intrinsic, robust error analysis [1,5,7,8,12,19]. Distinction of genuine from spurious resonances has been one of the thorniest challenges to MRS. Via the powerful concept of Froissart doublets, the FPT achieves this task, filtering out completely all spurious information from the final output data [14,17–19,25]. This new paradigm [17] is called "Signal-Noise Separation" and acronymed by SNS. Thus, for the first time the entire information about metabolites, including concentrations is obtained without guessing and this obviates the need for fitting with its attendant ambiguities that are clinically unacceptable.

The advantages of Padé-optimization were clearly demonstrated for MRS data from four problem areas within oncology: ovarian, breast and prostate cancer as well as brain tumors. We have applied the fast Padé transform to time signals associated with in vitro MRS data encoded from (a) malignant and benign ovarian lesions, (b) breast cancer, fibroadenoma and normal breast tissue and (c) for cancerous prostate, normal stromal and glandular prostate. Before, in each of these areas, while showing substantial potential, the diagnostic yield of MRS has been limited by the reliance upon the FFT with post-processing through fitting. As stated, not only does the FFT

have low resolution, but as a non-parametric method, it can only supply a total shape spectrum. Thus, no information is provided about the actual number of resonances present, and attempts at quantification via fitting the Fourier total lineshapes is highly problematic, particularly whenever the spectrum is tightly packed with structures, as is often the case.

The FPT applied to benign and malignant ovarian fluid, dramatically improved SNR and provided highly accurate determination of key metabolite concentrations for identifying ovarian cancer. These features of the FPT are deemed to be of critical benefit to ovarian cancer diagnostics via MRS, in particular for early detection, a goal which has thus far been elusive, and achievement of which would definitely confer a major survival advantage.

The results for MRS data from the cancerous breast, fibroadenoma and normal breast tissue, showed the advantages of the Padé-optimization, especially for areas of high spectral density. The FPT unequivocally resolves and precisely quantifies extremely closely lying resonances, including phosphocholine, a marker of malignant transformation of the breast. This line of investigation is being continued with other encoded data from benign and malignant breast tissue, both in vitro and in vivo. We anticipate that Padé-optimized MRS will reduce the false positive rates of MR-based modalities and further improve their sensitivity. Once this is achieved, and since MR entails no ionizing radiation, new possibilities for screening/early detection will open up, especially for risk groups, e.g. Padé-optimized MRS could be used with greater surveillance frequency among younger women at high breast cancer risk.

Spectral overlap with multiplet resonances is recognized to be very troublesome for MRS of the prostate [45]. Our results illustrate that the FPT can unequivocally resolve and accurately quantify a large number of overlapping resonances, including multiplets of metabolites that distinguish normal glandular prostate, normal stromal prostate and prostate cancer. MRS with the accompanying Padé quantification applied to prostate cancer is particularly important for diagnostic enhancement, because of the current dilemmas surrounding prostate cancer screening (e.g. cutpoints of prostate specific antigen (PSA)), as well as its public health importance.

MRS has made great strides in medicine by relying upon a mere handful of metabolites, or even a single metabolite, e.g. choline for breast cancer. This severely restricted metabolite window stems directly from the limitations of the FFT and subsequent post-processing via fitting and other related phenomenological approaches with adjustable parameters. It is expected that the diagnostic yield of MRS in oncology will be enhanced by extracting reliable information about many more metabolites. This is facilitated by the FPT, on the basis of its proven validity, theoretically supported by quantum physics and algorithmically confirmed by computations. This basic science input is needed, since the empirical/phenomenological approaches have been exhausted in this area. As a research field and a clinical diagnostic modality, MRS is undergoing a veritable renaissance. Starting from its status as the well-established nuclear magnetic resonance (NMR) in physics and analytical chemistry, MRS has developed to such a point in medicine that it is currently being viewed by experts as the modality which has the potential to revolutionize not only diagnostics, but also molecular-image guided surgery and target delineation for radiotherapy [49–53].

We have emphasized that there is an urgent need for accurate quantification to determine metabolite concentrations, so that MRS can be better used to detect and characterize cancers, with clear distinction from non-malignant processes. The FPT provides accurate quantification of time signals associated with in vitro data from ovarian, breast and prostate cancer as well as benign or normal tissue. We chose these problem areas because of their urgent clinical importance.

Extensive validation of the FPT has been performed on in vivo encoded MRS time signals from high field and clinical (1.5 T) scanners [1–7,9,19,22]. The FPT is thus now established as the method which can robustly handle MRS problems of key importance, i.e. separating noise from genuine signal, reconstructing completely overlapping resonances (brain, breast spectra), or very dense spectra with numerous multiplet resonances (prostate).

4.1 A link to radiation oncology and target planning

Magnetic resonance spectroscopy and MR spectroscopic imaging (MRSI) have been applied most extensively in radiation neuro-oncology. Molecular imaging through MRS and MRSI have been used to help define complex target geometries of brain tumors and to evaluate new contrast-enhancing lesions appearing after RT [19,22]. Distinction between recurrent glioma and radiation necrosis with the appearance of new contrast-enhancing lesions has been facilitated by MRSI. Most frequently, this has been based upon the ratio of Cho/Cr. We have performed a meta-analysis of all available published data comparing radiation necrosis and recurrent primary brain tumors in new contrast enhancing lesions post-RT. The ratio of Cho/Cr was significantly greater in the latter compared to the former. However, there was no ideal cut point which unequivocally identified recurrent tumor, such that up to 50% of the brain tumors could be mistaken for radiation necrosis [22]. As was illustrated in Figs. 1 and 9 of this paper, the accuracy of Cho/Cr metabolite ratios assessed using Fourier-based processing of MR time signals was called into question. In sharp contrast, the fast Padé transform accurately reconstructs the spectral parameters and thereby provides the means for reliably computing the metabolite concentrations that are needed not only for target definition, but also for follow-up, post-RT [22].

5 Conclusions

The results presented in this paper provide the basis for the needed next steps: to extensively apply the FPT to in vivo time signals encoded mainly on clinical scanners from e.g. brain tumors, breast, ovary and prostate cancers as well as from benign and normal tissue. Normative databases need to be developed for metabolite concentrations versus those for cancers. These will distinguish malignant versus benign disease with specific patterns of departures from normal metabolite concentrations. The overall goal is that this practical approach through mathematical optimization enables Padé-based MRS to soon be implemented in clinical oncology, including target planning, post-radiotherapeutic follow-up and other aspects of radiation therapy.

References

1. Dž. Belkić, *Quantum Mechanical Signal Processing and Spectral Analysis* (Institute of Physics Publishing, Bristol, 2005)
2. Dž. Belkić, K. Belkić, Phys. Med. Biol. **50**, 4385 (2005)
3. Dž. Belkić, Nucl. Instrum. Method Phys. Res. A **52**, 366 (2004)
4. K. Belkić, Dž. Belkić, J. Comput. Methods Sci. Eng. **4**, 157 (2004)
5. Dž. Belkić, Nucl. Instrum. Method Phys. Res. A **525**, 379 (2004)
6. Dž. Belkić, Nucl. Instrum. Method Phys. Res. A **525**, 372 (2004)
7. Dž. Belkić, Phys. Med. Biol. **51**, 2633 (2006)
8. Dž. Belkić, Phys. Med. Biol. **51**, 6483 (2006)
9. Dž. Belkić, K. Belkić, Phys. Med. Biol. **51**, 1049 (2006)
10. Dž. Belkić, Adv. Quantum Chem. **51**, 157 (2006)
11. K. Belkić, Nucl. Instrum. Method Phys. Res. A **580**, 874 (2007)
12. Dž. Belkić, Nucl. Instrum. Method Phys. Res. A **580**, 1034 (2007)
13. Dž. Belkić, K. Belkić, J. Math. Chem. **43**, 395 (2008)
14. Dž. Belkić, K. Belkić, J. Math. Chem. **44**, 887 (2008)
15. Dž. Belkić, K. Belkić, J. Math. Chem. **45**, 790 (2009)
16. Dž. Belkić, K. Belkić, J. Math. Chem. **45**, 819 (2009)
17. Dž. Belkić, Adv. Quantum Chem. **56**, 95 (2009)
18. Dž. Belkić, K. Belkić, J. Math. Chem. **45**, 563 (2009)
19. Dž. Belkić, K. Belkić, *Signal Processing in Magnetic Resonance Spectroscopy with Biomedical Applications* (Taylor & Francis, London, 2010)
20. Dž. Belkić, Adv. Quantum Chem. **62**, 145 (2011)
21. K. Belkić, Dž. Belkić, Isr. Med. Assoc. J. **13**, 236 (2011)
22. Dž. Belkić, K. Belkić, Molecular imaging and magnetic resonance for improved target definition in radiation oncology. Radiat. Damage Biomol. Syst. (2011, in press)
23. Dž. Belkić, K. Belkić, Adv. Quantum Chem. **62**, 243 (2011)
24. Dž. Belkić, K. Belkić, J. Phys. B **44**, 125002 (2011)
25. Dž. Belkić, K. Belkić, J. Phys. B **44**, 125003 (2011)
26. Dž. Belkić, K. Belkić, Int. J. Quantum Chem. **105**, 493 (2005)
27. D.S. Stephenson, Prog. NMR Spectrosc. **20**, 515 (1988)
28. W. Pijnappel, A. van den Boogaart, R. de Beer, D. van Ormondt, J. Magn. Reson. **97**, 122 (1992)
29. J.W. van der Veen, R. de Beer, P.R. Luyten, D. van Ormondt, Magn. Reson. Med. **6**, 92 (1988)
30. L. Vanhamme, A. van den Boogaart, S. van Haffel, J. Magn. Reson. **29**, 35 (1997)
31. S.W. Provencher, Magn. Reson. Med. **30**, 672 (1993)
32. J. Frahm, H. Bruhn, M.L. Gyngell, K.D. Merboldt, W. Hanicke, R. Sauter, Magn. Reson. Med. **9**, 79 (1989)
33. I. Tkáč, P. Andersen, G. Adriany, H. Merkle, K. Ugurbil, R. Gruetter, Magn. Reson. Med. **46**, 451 (2001)
34. Dž. Belkić, I. Mančev, J. Hanssen, Rev. Mod. Phys. **80**, 249 (2008)
35. Dž. Belkić, Adv. Quantum Chem. **56**, 251 (2009)
36. M.M. Sant'Anna, A.C.F. Santos, L.F.S. Coelho, G. Jalbert, N.V. de Castro Faria, F. Zappa, P. Focke, Dž. Belkić, Phys. Rev. A **80**, 042707 (2009)
37. Dž. Belkić, J. Math. Chem. **47**, 1366 (2010)
38. Dž Belkić, J. Math. Chem. **47**, 1420 (2010)
39. Dž. Belkić, *Fast Collisions of Light Ions with Matter* (World Scientific Publishers, Singapore, 2011, in press)
40. E. Boss, S.H. Moolenaar, L.F.A.G. Massuger, H. Boonstra, U.F.H. Engelke, J.G.N. de Jong, R.A. Wevers, NMR Biomed. **13**, 297 (2000)
41. I. Gribbestad, B. Sitter, S. Lundgren, J. Krane, D. Axelson, Anticancer Res. **19**, 1737 (1999)

42. E. Aboagye, Z. Bhujwalla, Cancer Res. **59**, 80 (1999)
43. R. Katz-Brull, D. Seger, D. Rivenson-Segal, E. Rushkin, H. Degani, Cancer Res. **62**, 1966 (2002)
44. K. Glunde, C. Jie, Z. Bhujwalla, Cancer Res. **64**, 4270 (2004)
45. M. Swanson, A. Zektzer, Z. Tabatabai, J. Simko, S. Jarso, K. Keshari, L. Schmitt, P. Carroll, K. Shinohara, D. Vigneron, J. Kurhanewicz, Magn. Reson. Med. **55**, 1257 (2006)
46. J.K. Nicholson, I.D. Wilson, Prog. NMR Spectrosc. **21**, 449 (1989)
47. T. Schirmer, D.P. Auer, NMR Biomed. Priv. Commun. **13**, 28 (2000)
48. B.J. Soher, R.E. Hurd, N. Sailasuta, P.B. Barker, Magn. Reson. Med. **36**, 335 (1996)
49. C.E. Mountford, S. Doran, C.L. Lean, P.L. Russell, Chem. Rev. **104**, 3677 (2004)
50. L. Kwock, J. Smith, M. Castillo, M. Ewend, F. Collichio, D. Morris, T. Bouldin, S. Cush, Lancet Oncol. **7**, 859 (2006)
51. G. Tse, D. Yeung, A. King, H. Cheung, W. Yang, Breast Cancer Res. Treat. **104**, 249 (2007)
52. C.K. Kuhl, W. Kuhn, H. Schild, Breast **14**, 480 (2005)
53. R. Huzjan, E. Sala, H. Hricak, Nat. Clin. Pract. Urol. **2**, 434 (2005)
54. J. Evelhoch, M. Garwood, D. Vigneron, M. Knopp, D. Sullivan, A. Menkens, L. Clarke, G. Liu, Cancer Res. **65**, 7041 (2005)